The Indo-Australian monsoon and its relationship to ENSO and IOD in reanalysis data and the CMIP3/CMIP5 simulations

Author:
Jourdain, Nicolas; Sen Gupta, Alexander; Taschetto, Andrea; Ummenhofer, C; Moise, A; Ashok, K

Publication details:
Climate Dynamics
v. 41
Chapter No. 11-12
pp. 3073-3102
0930-7575 (ISSN)

Publication Date:
2013

Publisher DOI:
http://dx.doi.org/10.1007/s00382-013-1676-1

Climate Dynamics

The Indo-Australian monsoon and its relationship to ENSO and IOD in reanalysis data and the CMIP3/CMIP5 simulations

--Manuscript Draft--

Manuscript Number:	
Full Title:	The Indo-Australian monsoon and its relationship to ENSO and IOD in reanalysis data and the CMIP3/CMIP5 simulations
Article Type:	Original Article
Keywords:	Indian monsoon; Australian monsoon; Maritime Continent; ENSO; IOD; CMIP5; CMIP3; monsoon projection
Corresponding Author:	Nicolas C. Jourdain University of New South Wales Sydney, NSW AUSTRALIA
Corresponding Author Secondary Information:	
Corresponding Author's Institution:	University of New South Wales
Corresponding Author's Secondary Institution:	
First Author:	Nicolas C. Jourdain
First Author Secondary Information:	
Order of Authors:	Nicolas C. Jourdain
	Alexander Sen Gupta
	Andréa S Taschetto
	Caroline C Ummenhofer
	Aurel F Moise
	Karumuri Ashok
Order of Authors Secondary Information:	
Abstract:	A large spread exists in both Indian and Australian average monsoon rainfall and in their interannual variations diagnosed from various observational and reanalysis products. While the multi model mean monsoon rainfall from 60 models taking part in the Coupled Model Intercomparison Program (CMIP3 and CMIP5) fall within the observational uncertainty, considerable model spread exists. Rainfall seasonality is consistent across observations and reanalysis, but most CMIP models have biases in monsoon season duration, with CMIP5 models generally performing better than CMIP3. Most models reproduce the observed ENSO-Australian monsoon teleconnection, with the strength of the relationship dependent on the strength of the simulated ENSO. However, over the Maritime Continent, the monsoon-ENSO connection is generally weaker than observed, depending on the ability of each model to realistically reproduce the ENSO signature in the Warm Pool region. The Indian monsoon-ENSO relationship is affected by overly persistent ENSO events in many CMIP models. It is also shown that models with stronger monsoon-ENSO relationships generally have a stronger monsoon-IOD relationship. Based on model fidelity in reproducing realistic monsoon characteristics and ENSO teleconnections, we objectively select 13 "best" models to analyze projections in the rcp8.5 scenario. Twelve of these models are from the CMIP5 ensemble. In India and Australia, most of these models produce 5 to 20% more monsoon rainfall over the 21st century than during the pre-industrial period. By contrast, there is no clear model consensus over the Maritime Continent.

The Indo-Australian monsoon and its relationship to ENSO and IOD in reanalysis data and the CMIP3/CMIP5 simulations

Nicolas C. Jourdain[1], Alexander Sen Gupta[1],

Andréa S. Taschetto[1], Caroline C. Ummenhofer[2],

Aurel F. Moise[3], Karumuri Ashok[4]

26 July 2012

[1] Climate Change Research Centre, University of New South Wales, Sydney, Australia

[2] Department of Physical Oceanography, Woods Hole Oceanographic Institution, Woods Hole, MA, USA

[3] Centre for Australian Weather and Climate Research, Bureau of Meteorology, Melbourne, Australia

[4] Centre for Climate Change Research, Indian Institute of Tropical Meteorology, Pune, India

Corresponding author :

nicolas_jourdain@yahoo.fr

Abstract

A large spread exists in both Indian and Australian average monsoon rainfall and in their interannual variations diagnosed from various observational and reanalysis products. While the multi model mean monsoon rainfall from 60 models taking part in the Coupled Model Intercomparison Program (CMIP3 and CMIP5) fall within the observational uncertainty, considerable model spread exists. Rainfall seasonality is consistent across observations and reanalysis, but most CMIP models have biases in monsoon season duration, with CMIP5 models generally performing better than CMIP3.

Most models reproduce the observed ENSO-Australian monsoon teleconnection, with the strength of the relationship dependent on the strength of the simulated ENSO. However, over the Maritime Continent, the monsoon-ENSO connection is generally weaker than observed, depending on the ability of each model to realistically reproduce the ENSO signature in the Warm Pool region. The Indian monsoon-ENSO relationship is affected by overly persistent ENSO events in many CMIP models. It is also shown that models with stronger monsoon-ENSO relationships generally have a stronger monsoon-IOD relationship.

Based on model fidelity in reproducing realistic monsoon characteristics and ENSO teleconnections, we objectively select 13 ”best” models to analyze projections in the rcp8.5 scenario. Twelve of these models are from the CMIP5 ensemble. In India and Australia, most of these models produce 5 to 20% more monsoon rainfall over the 21stcentury than during the pre-industrial period. By contrast, there is no clear model consensus over the Maritime Continent.

1 Introduction

The mechanisms that drive changes in the Indo-Pacific summer monsoon system are of considerable interest as this phenomenon affects many human activities and resources over broad areas. The Indo-Australian monsoon consists of the Indian and South-East Asian summer monsoon that occurs from June to September (JJAS), and of the monsoon that occurs in austral summer (December to March, DJFM) over Australian and Maritime Continent (Neale and Slingo, 2003). Contrary to popular understanding, the Australian and Maritime Continent monsoon does not appear to be primarily driven by land-ocean temperature contrast (Yano and McBride, 1998; Chao and Chen, 2001), and the importance of land-ocean contrast for the Indian monsoon is still a matter of debate (Liu and Yanai, 2001; Chao and Chen, 2001). The presence of the Himalaya, however, plays a key role in the Indian Monsoon, essentially by insulating warm moist air over India from cold dry air further North (Boos and Kuang, 2010).

On interannual timescales, the India-averaged monsoon rainfall tends to be relatively weak when it co-occurs with the development of an El Niño, and vice versa for La Niña. Other sea surface temperature (SST) patterns such as the Arabian Sea upwelling (Izumo et al., 2008) also seem to affect the regional distribution of monsoon within India on interannual timescales (Mishra et al., 2012). This picture is complicated by the Indian Ocean Dipole (IOD, Saji et al., 1999) that modulates ENSO influence on the Indian summer monsoon (Ashok et al., 2001; Ummenhofer et al., 2011). Australian monsoon rainfall also tends to be weak during El Niños (Holland, 1986). The positive phase of the IOD (that peaks in September-November, SON) also tends to weaken the following monsoon over the Australian/Maritime continent (Cai et al., 2005).

For the combined Indo-Australian monsoon system, Meehl (1997) and Meehl and Arblaster (2002) have described a tropospheric biennial oscillation (TBO) that seems to link the Indian and the Australian monsoons through ocean-atmosphere coupled mechanisms.

On longer timescales, the impact of climate change on the monsoon system is a major concern. Climate change may directly affect the monsoon in two compensating ways: 1- warmer SSTs enable more evaporation and tend to increase the monsoon strength 2- SSTs warm more in the equatorial region than in the Tropics, which tends to weaken the monsoon circulation (Chung and Ramanathan, 2006; Krishnan et al., 2012). These two mechanisms are tightly linked to possible change in SST global modes of variability, in particular ENSO (El Niño Southern Oscillation) and the IOD (Indian Ocean Dipole) (Shi et al., 2008; Zhang et al., 2012). Other factors may also influence the monsoon, as, for instance, the upper tropospheric properties (Rajendran et al., 2012).

Over the last few years, the ability of general circulation models (GCMs) to realistically simulate the Indo-Pacific monsoon and its teleconnections has been analyzed in the context of the Coupled Model Intercomparison Program 3 (CMIP3), contributing to the Intergovernmental Panel on Climate Change (IPCC) Fourth Assessment Report (IPCC, 2007). While the link between ENSO and the Australian monsoon rainfall is rather well captured by the CMIP3 models (Colman et al., 2011), the ENSO-rainfall relationship is poorly captured near Papua-New Guinea (Cai et al., 2009). These authors have suggested that the ENSO-rainfall relationship is affected by the so called "cold tongue bias" where SST is too cold along the equator, and positive SST anomalies extend too far West during El Niño events (with a significant impact on the Maritime Continent rainfall). In the CMIP3 ensemble, there is no model consensus on how interannual variability of tropical Australian precipitation will change in future climate (Moise et al., 2012). By contrast, a clear increase of future monsoon rainfall has been found over the Maritime Continent (Smith et al., 2012). Finally, based on the CMIP3 models, the South-East Asian summer monsoon is likely to undergo a slight increase of precipitation in the future (IPCC, Meehl et al., 2007).

In this paper, we evaluate the Indo-Australian monsoon and its teleconnections to ENSO and IOD in the CMIP simulations. We perform a combined analysis of simulations from 24 CMIP3 models and from 35 models taking part in the new Coupled Model Intercomparison Program 5 (CMIP5). Results from 7 atmospheric reanalysis are also included as reanalysis are often used as a proxy for dynamical observations (e.g. wind, pressure) to evaluate the CMIP model dynamics, or to analyze mechanisms. Precipitation provides an integrated assessment of the reanalysis skills (atmospheric model and data assimilation system) since rainfall observations are generally not assimilated in the system (see section 2.2). Finally, we select a subset of models that represent the Indo-Australian monsoon and its connections to ENSO well, and we assess projected change in monsoon rainfall during the 21^{st}century.

2 Datasets

2.1 Indices definition

To get an overview of the models skill, we use box-averaged indices rather than maps. We use two land-only monsoon rainfall indices for Australia and India (LAUS and LIND, Tab. 1, Fig. 1), as land-based rainfall has a direct influence on many human activities and resources, and because long-term rainfall data are only available over the land. Two other monsoon indices are also examined: AMAR and ISAS (Tab. 1, Fig. 1) that include rainfall over ocean and land over a larger domain. These indices are potentially better suited to examine climate teleconnections and have been used previously to examine the TBO (e.g. Meehl and Arblaster, 2002).

In addition, standard SST indices are used to describe the major tropical modes of variability in the Indo-Pacific region (ENSO and IOD, see Tab.1 and Fig.1). It could be argued that indices based on fixed locations may not fully capture the model dynamics since simulated variability may have spatial biases compared to observations. However, it is also important to capture modes of variability at realistic locations as this may affect the propagation of teleconnection patterns to remote regions (Taschetto et al., 2009). For ENSO, most of the CMIP3 models are not able to realistically reproduce distinct central Pacific El Niño (also referred to as Modoki, or Warm Pool El Niño) and canonical El Niño (also referred to as Cold Tongue El Niño) (Yu and Kim, 2010). Thus, CMIP3 models produce too much coherence between NINO3, NINO34 and the El Niño Modoki Index (Cai et al., 2009). The models skills concerning the representation of these two kinds of ENSO have improved in CMIP5 (Kim and Yu, 2012; Taschetto et al., 2012). A majority of the CMIP3 and CMIP5 models still fail to capture the variance associated with these statistical modes realistically (Roxy et al., 2012; Shamal et al. 2012, under preparation). For these reasons, we decide to use the NINO34 index in this paper. It captures both kinds of ENSO without giving too much importance to strong East Pacific (canonical) El Niño. The later have indeed been suggested to have a weaker influence on the Indo-Australian monsoon than the central Pacific El Niño (e.g. Taschetto and England, 2009; Kumar et al., 2006). For the IOD, Cai et al. (2009) have shown that most of the CMIP3 models produce a SST dipole pattern that is similar to observed, even though the amplitude of the cold tongue varies from model to model (their Fig.10). Therefore, the simulated Indian Ocean Dipole Mode Index (DMI, as defined by Saji and Yamagata, 2003) makes a reasonable index to represent the model IOD.

In this work, all the diagnostics related to the interannual variability of an index are made after removal of the trend (linear least mean square fit) and of the climatological seasonal cycle.

2.2 Observation-based products and reanalysis

In this paper, we analyze precipitation data from 7 atmospheric reanalysis (lower part of Tab.1) and from gridded observational products (upper part of Tab.1). Some gridded observational products, such as GPCP, CMAP and TRMM-3B43, merge gauge analysis and satellite observations (available since the late 1970s). Before the satellite era, rainfall data are only available to any significant extent over land, and based on station measurements (GPCC, AWAP, APHRODITE). There are significant differences in the observation datasets, due to retrieval methods, treatments of uncertainties, and quality check (e.g. Yin et al., 2004).

Among the 7 atmospheric reanalysis, only ERAinterim uses a 4D-VAR data assimilation scheme; the others use a 3D-VAR scheme. Rainfall from the various reanalysis is purely model-generated (i.e. a forecast), since observed rainfall is not assimilated (see references in Tab.1). An exception is MERRA whose atmospheric data assimilation has been developed with a special focus on the hydrological cycle. While reanalysis generally show some skills in reproducing the observed seasonal and interannual variability, their accuracy varies significantly across the regions (Bosilovich et al., 2008). Uncertainties in reanalyzed precipitation may come from limitations in the dynamical models (e.g. convection, cloud microphysics, complex topography), from uncertainties in the observations, and from the data assimilation scheme itself.

The interannual variability of the various rainfall datasets for summer monsoon seasons is compared to the observed variability in the Taylor Diagram in Fig. 2. Over Australia, the AWAP dataset is generally considered as a reference, while the APHRODITE dataset is chosen as a reference for South Asia and India because it has been developed with a special focus on this region. These two datasets are based on weather stations, as is GPCC, and cover a long time period. In general the observation and reanalysis datasets are more consistent over Australia. The spread of reanalysis precipitation is larger for the Indian monsoon, with outliers like NCEP-CFSR and, to a lower extent, NCEP-DOE-II. All the observation products are correlated to AWAP by at least 0.95 in Australia. Correlation coefficients between observations and APHRODITE are much lower over India, with, for instance, CMAP being correlated to APHRODITE by 0.66. Note that 3B43 and 3B42 are only weakly correlated to APHRODITE, but the overlap is only 10 years (their correlation to GPCC is greater than 0.9 over the period 1998-2011). The correlation coefficient between reanalysis and AWAP/APHRODITE is in the range 0.85-0.95 in Australia, and 0.35-0.85 in India. It is possible that this difference in consistency between India and Australia could be related to the Himalaya whose influence on the atmosphere is difficult to simulate, and where in-situ observations are sparse and difficult to assimilate. A stronger influence of SST for the Australian monsoon compared to the Indian monsoon may also improve consistency in the reanalysis given that they are forced by observed SST.

Two SST datasets are used in this paper, HadISST and HadSST2 (Tab. 1). HadSST2 has a coarser (5-degree) resolution than HadISST, but no interpolation is used to fill grid points where observations are missing. As both datasets lead to similar results, only results from HadISST are shown here. For the sake of consistency, we also use SST from reanalysis when we produce diagnostics mixing SST and precipitation. It is important to keep in mind that the reanalysis use prescribed ocean SST, except for NCEP-CFSR which has a coupled ocean component.

2.3 CMIP3 and CMIP5 simulations

In this paper, we first analyze 24 CMIP3 simulations (Tab. 3) and 35 CMIP5 simulations (Tab. 4) based on the historical simulations (called *20C3M* in CMIP3 and *historical* in CMIP5). The simulations start approximately in 1850 and end in approximately 2000 and 2005 for CMIP3 and CMIP5 respectively. The CMIP3 models and experiments have been widely described in the literature over the last 5 years (e.g. Randall et al., 2007). Some institutes have increased the resolution of their models from CMIP3 to CMIP5 (e.g. CNRM, GISS, INMMRI). From CMIP3 to CMIP5 a large number of new experiments have been included (Taylor et al., 2011). Some experiments now include a biogeochemical component accounting for carbon cycles in the land, atmosphere, and ocean (Earth System Models, see "ESM" in model names of Tab. 4). It should be noted, however, that the historical experiment has prescribed gas concentrations (including CO_2). Some of the CMIP3 and CMIP5 models have repeated historical (and future) experiments to form an ensemble with different initial conditions (the initial state is taken in different points of the pre-Industrial simulation).

In section 3.3, we use a limited number of CMIP5 simulations to examine a future greenhouse gas and aerosols emission scenario. We use the representative concentration pathway rcp8.5 (Moss et al., 2010; Riahi et al., 2011). This scenario corresponds to a radiative forcing of approximately 8.5 $W.m^{-2}$ higher in 2100 than in the pre-industrial period. This is the most extreme scenario used to constrain the CMIP5 simulations in the sense that energy and industrial CO_2 emissions increase continuously until at least 2100 (whereas such emissions decrease from $\sim$ 2080 in rcp6.0 and from $\sim$ 2050 in rcp4.5).

Where we present information based on multi-model means, we first average across ensemble members of a given model, before averaging across the models. Where we consider correlations between several model results, we assume that each model is different enough to be considered independent (we thus probably over-estimate the significance since some models are not strictly independent). A few of the CMIP3 models included water only (inmcm3-0) or water and heat (mri-cgcm2-3-2a, miub-echo-g, cgcm3 T47 and T63) flux adjustment. Finally, some institutes have produced simulations from two models run at two different resolutions (subscript LR/MR in model names of Tab. 3, 4), different cloud/convective parameterization in the atmosphere model (e.g. IPSL-CM5A/IPSL-CM5B), or different ocean models (e.g. GFDL-ESM2M/GFDL-ESM2G). In such cases, the two models are considered separately, as independent models. Similarly, we consider that the CMIP3 version of a model is independent from the CMIP5 version (e.g. gfdl-cm2-0/GFDL-CM3), and we even refer to these two versions as "two models" in the following.

The acronyms used to refer to the institutes in Tab. 3 and Tab. 4 stand for the Environment Research & Technology Development Fund of the Ministry of the Environment, Japan (ERTDF), the Commonwealth Scientific and Industrial Research Organisation (CSIRO), the Bureau of Meteorology (BOM), the Beijing Climate Center (BCC) of the China Meteorological Administration (CMA), the Canadian Centre for Climate Modelling and Analysis (CCCMA), the Centro Euro-Mediterraneo per I Cambiamenti Climatici (CMCC), the National Center for Atmospheric Research (NCAR), the Centre National de Recherches Meteorologiques (CNRM) of Meteo-France, the European Centre for Research and Advanced Training in Scientific Computa-

tion (CERFACS), the Queensland Climate Change Centre of Excellence (QCCCE), the European Centre for Medium-Range Weather Forecasts (ECMWF), the The National Key Laboratory of Numerical Modeling for Atmospheric Sciences and Geophysical Fluid Dynamics (LASG), the Institute of Atmospheric Physics (IAP) of the Chinese Academy of Sciences, the China Environmental Science and Sustainability Research Group (CESS), the Tsinghua University (THU), the National Oceanic and Atmospheric Administration (NOAA), the Geophysical Fluid Dynamics Laboratory (GFDL), the National Aeronautics and Space Administration (NASA), the Goddard Institute for Space Studies (GISS), the Met Office Hadley Centre (MOHC), National Institute of Meteorological Research (NIMR), the Korea Meteorological Administration (KMA), the Institute for Numerical Mathematics in Moscow (INM), the Institut Pierre Simon Laplace (IPSL), the Atmosphere and Ocean Research Institute (AORI) at the University of Tokyo, the National Institute for Environmental Studies (NIES), the Japan Agency for Marine-Earth Science and Technology (JAMSTEC), the Max Planck Institute for Meteorology (MPI-M), the Meteorological Research Institute (MRI), and the Norwegian Climate Centre (NCC).

3 Results

We first evaluate the mean summer monsoon rainfall, the amplitude of interannual variability, and the seasonal cycle in each model and reanalysis (section 3.1). Then, we assess the representation of the monsoon-ENSO and monsoon-IOD relationships (section 3.2). Based on these results, we select the most realistic models, and we show future projections of the monsoon (section 3.3).

3.1 Statistical properties of the historical Indo-Australian monsoon

The mean Indian and Australian summer monsoon rainfall is presented for each model and reanalysis in Fig. 3-a. The spread in the observed mean summer monsoon rainfall is quite large. For instance, the mean JJAS LIND is 6.8 mm/day in GPCC, versus 5.5 mm/day in APHRODITE. Furthermore, the uncertainty in the mean rainfall in reanalysis is very similar to the uncertainty in observations. We therefore choose to consider the multi observation/reanalysis mean (black triangle in Fig. 3-a) as our reference here, with an uncertainty envelope given by the two-dimensional PDF (Probability Density Function) of observations and reanalysis (see caption of Fig. 3). The mean DJFM Australian monsoon rainfall based on the multi-model mean is very similar to observational estimates in both the CMIP3 and the CMIP5 models (triangles in Fig. 3-a). The mean JJAS Indian monsoon rainfall based on the multi-model mean is under-estimated by $\sim 15\%$ in CMIP3, and by $\sim 19\%$ in CMIP5 (Fig. 3-a), though it lies within the 75% envelope of the observations/reanalysis. In both CMIP3 and CMIP5 simulations, the relatively good skill of the multi-model mean hides a wide spread in the mean monsoon rainfall, across individual CMIP3 and CMIP5 models: from nearly no rainfall to twice as much rain as observed. The spread, as estimated by the standard deviation, is 20% higher in the CMIP5 than the CMIP3 models for LIND, but 7% smaller for LAUS. Finally, there is a significant correlation between the average monsoon rainfall in India, and that in Australia ($r=0.56$, $p < 0.0001$) which suggests that discrepancies between models and observations are related to intrinsic model performance (e.g. convective scheme, land surface scheme), not only to regional issues in the models.

The amplitude of the interannual variability is now evaluated through the standard deviation of summer-months-averaged rainfall, and presented in Fig. 3-b. The spread in the observed values is larger here than for the mean, and has already been discussed for non-detrended time series in section 2.2. Due to this spread, we still consider the multi observation/reanalysis mean as a reference, with an uncertainty envelope given by the PDF. We nonetheless exclude two outliers from the multi observation/reanalysis mean and envelope calculation: NCEP-CFSR and NCEP-DOE-II (represented by μ), because these two reanalysis present a much stronger interannual variability than any other reanalysis or observation dataset. The standard deviation of both the Indian and the Australian monsoon rainfall based on the multi-model mean is in remarkably good agreement with observations in CMIP3 and CMIP5 (triangles in Fig. 3-b). This again hides a wide spread in the simulated amplitude of the interannual variability in both CMIP3 and CMIP5. The spread, as measured by the standard deviation, is very similar in CMIP3 and CMIP5 for LIND, but 30% higher in CMIP3 than in CMIP5 for LAUS. Finally, there is a significant correlation coefficient between the amplitude of the monsoon interannual variability in India and that in Australia ($r=0.52$, $p < 0.0001$). This is probably related to the fact that there are common drivers affecting the amplitude of the Indian and of the Australian monsoon (e.g. ENSO).

For both the Indian and the Australian monsoons, the correlation between the mean and the interannual variability is relatively weak ($r=0.12$ for LIND and $r=0.36$ for LAUS). This emphasizes the importance of evaluating a model both with regard to its mean and its variability. For instance, the CMIP5 experiment from GFDL-ESM2M (represented by R) has a realistic mean Australian monsoon rainfall, but its interannual variability is far too strong.

As many modes of climate variablity are phase-locked to the seasonal cycle, we also evaluate the later for each CMIP model in Fig. 4. By contrast to the mean and to the interannual variability, the seasonal cycle is robust across the observations and reanalysis (see the small RMS errors in Fig. 3-c and 4). Based on the multi-model mean seasonal cycle, there is a clear improvement from the CMIP3 to the CMIP5 simulations (the RMS error is reduced by 25-30%, see triangles in Fig. 3-c). However, the simulated seasonal cycle are generally either too peaked in February (e.g. IPSL-CM5B-LR), or have an overly indistinct monsoon season with high rainfall extending into April-May and October-November (e.g. CCSM4). The maximum generally occurs on the right month, despite a few exceptions as mpi-echam5 (Fig. 4). In the 20 CMIP simulations that best represent the seasonal cycles (ranked by RMSE in Fig. 4), only 4 (3) are from CMIP3 for LAUS (LIND). It should also be noted that the best CMIP3 model both for LIND and LAUS (mri-cgcm2-3-2a, represented by t) has both heat and water flux corrections. Finally, there is also a significant correlation coefficient between the amplitude of the RMSE of the simulated seasonal cycle in India and that in Australia ($r=0.55$, $p < 0.0001$).

A first model selection is made, based on the three statistical properties of the Indo-Australian monsoon depicted in Fig. 3. As mentioned above, the mean summer monsoon rainfall and its interannual variability show a significant spread in the observations. We take this into account, and select the models that are within the contour enclosing 99.9% of the observations/reanalysis PDF integrative (blue contour in Fig. 3-a,b). This value is found empirically, in such a way to keep a sufficient number of models in the selection process. We do the same selection with regards to the seasonal cycle (Fig. 3-c), except that we extend the contour so that it encloses 99.999% of the observations/reanalysis PDF integrative. This extension is needed because the spread in the observed/reanalyzed seasonal cycle is very weak, and because the CMIP simulated seasonal cycles are significantly distinct from the observed ones. Our overall method of selection allows eliminating models based on the observations, taking uncertainty into account. Using the contour values mentioned above leads to a selection of 19 models that are indicated in Tab. 5. Only one of these 19 models (gfdl-cm2-0) is from the CMIP3 ensemble. It should be noted that these models are not entirely independent because some components are commonly used in several models. For instance, CESM1-CAM5, CESM1-FASTCHEM, CCSM4, FIO-ESM, NorESM1-M, and NorESM1-ME include an atmospheric component based on the NCAR Community Atmospheric Model (CAM), even though versions differ across the institutes. The Hadley Centre atmospheric model is also the base of the atmospheric component in ACCESS1-0, Had-CM3, and HadGEM2-AO. The models ACCESS1-0, GFDL-CM3, and gfdl-cm2-0 have an ocean component based on the GFDL Modular Ocean Model (MOM). Finally, the Parallel Ocean Program (POP), which originated from the same historical base as MOM in the 1990s, is also a common base for the ocean component in CESM1-CAM5, CESM1-FASTCHEM, and CCSM4.

3.2 Relationship between SST modes and the Indo-Australian monsoon

As mentioned in the Introduction, the effect of greenhouse gases and aerosols on the Indo-Pacific monsoon will be modulated by ENSO and the IOD. Therefore, it is essential to have a realistic representation of the monsoon-ENSO and monsoon-IOD relationships in the historical experiments. This is analyzed in the present sub-section, starting with the Australian monsoon-ENSO relationship. The TRMM observational products 3B42 and 3B43 are not shown here, given the short record period.

Australian monsoon-ENSO relationship

Both the CMIP3 and the CMIP5 simulations show a moderate anti-correlation (-0.3) to NINO34 (Fig. 5-a), i.e. an Australian monsoon occurring during an El Niño event tends to be weaker than normal. This anti-correlation is significant at the 90% level for most of the CMIP3 and CMIP5 models (see upper quartiles), and is in good agreement with long observation timeseries (GPCC or AWAP, and HadISST, also already noted by Holland, 1986). Each model is shown separately in Fig. 6-a. As noted by Colman et al. (2011), a few CMIP3 models do not show significant ENSO-monsoon relationship at zero lag (*e.g.* giss models), while several CMIP3 simulations (*e.g.* csiro-mk3-5) produce too strong an anti-correlation at zero lag. This is still the case in the CMIP5 simulations, but correlations at zero lag are generally closer to GPCC and AWAP values. Thus, 33% of the CMIP3 models produce correlations in the range ± 0.1 of the observed correlation coefficient (-0.35), while 46% of the CMIP5 models do so. Surprisingly, this score is not better for the reanalysis, since only 3 of 7 are in this ± 0.1 range (NCEP-CFSR, NCEP-NCAR-I, and MERRA). Cai et al. (2009) demonstrated that in the CMIP3 simulations, models which produce an ENSO with a strong interannual variability tend to have a strong rainfall-NINO34 anti-correlation at zero lag. This is also what we find considering CMIP3 and CMIP5 models together (see pink line and circles in Fig. 6-b). A few models, in particular from the CMIP3 ensemble, show that a strong monsoon is followed, one year after, by an El Niño event (vice versa for La Niña). This is probably generally attributed to the fact that some CMIP3 models produce an ENSO with too strong a quasi-biennial component (e.g. gfdl-cm2-0 and miub-echo-g, Fig. 6-b).

An interesting feature in Fig. 5-a is the anti-correlation peak (-0.15) that is found in the multi observations/reanalysis mean 2 years prior to the monsoon, but which is totally absent from the CMIP simulations. When considering AWAP only over 100 years (dashed blue curve), this peak is reduced by half and far from significant at the 90% level. This peak is nonetheless interesting because it is opposite as what is expected from ENSO, since the later is anti-correlated with itself 1.5-2.5 years before (Fig. 5-d). As ENSO has been suggested to have a strong inter-decadal to centennial variability (Wittenberg, 2009), we raise the question as to whether such a peak can be captured by the models over a 30-year period. We extract the 30-year period from each 150-year simulation among the several available ensemble members that gives the strongest anti-correlation at year-2. As shown in Fig. 5-c, most of the CMIP models are able to simulate at least one 30-year period presenting an anti-correlation peak similar to the observed one. We therefore suggest that this peak is an artifact originating from the low frequency variability. Over such 30-year periods, the probability of Australia to Australia successful TBO transition is slightly increased (not shown), though the predictability associated with this transition remains non significant (not shown, see also Li et al., 2012).

We now expand the region used to define the Australian monsoon, by including the Maritime Continent (land and ocean, see Fig. 1). The relationship between ENSO and monsoon rainfall is now stronger: the anti-correlation between AMAR and the concomitant NINO34 is -0.6 for the multi observations/reanalysis mean (Fig. 5-b), and even reaches -0.8 for CMAP and GPCP (Fig. 7-a). All the reanalysis have strong anti-correlations (moderately strong for NCEP-NCAR-I and ERA40), which is consistent with an oceanic control of the monsoon in this region as most of the reanalysis are forced by observed SST. It should nonetheless be noted that shorter observational records are involved over the Maritime Continent (limited to the satellite era). Such strong anti-correlations are generally not reached in CMIP simulations, with a multi-model mean of -0.1 and -0.3 for the CMIP3 and the CMIP5 models respectively (Fig. 5-b). The CMIP5 models thus have better skills in capturing the AMAR-ENSO relationship, and more than 25% of CMIP5 models give anti-correlations that reach the range of reanalysis (see lower quartiles in Fig. 5-b). Comparing Fig. 7-a and 7-b, it is clear that most models that reproduce the observed AMAR-ENSO concomitant anti-correlation also simulate a realistic ENSO pattern along the equator, with a cold anomaly in the climatological warm pool region (*i.e.* approximately at the location of the Maritime Continent). This result is not surprising for this maritime region where convection is triggered by warm SSTs. Catto et al. (2012) have shown that only a few of the CMIP3 models are able to simulate a realistic relationship between NINO34 and SST North of Australia. Among their models, gfdl-cm2-0 has been shown to have the best skills. This is also what we find in Fig. 7-b, if we exclude csiro-mk3-5 which produces an unrealistic ENSO pattern as well as an unrealistic correlation between AMAR and ENSO 2 years in advance. Apart from these two CMIP3 models, the 19 CMIP models giving the strongest AMAR–NINO34 anti-correlation (< -0.36) are from CMIP5.

Indian monsoon-ENSO relationship

We now evaluate the Indian monsoon-ENSO relationship. As shown in Fig. 8-a,b, the Indian and South-Asian monsoons tend to be weak when their development is concomitant with the development of an El Niño, and vice versa for La Niña. The correlation between the land-based Indian JJAS rainfall (LIND) and NINO34 reaches -0.60 in APHRODITE, and -0.45 in the multi observations/reanalysis mean. The same correlation but for ISAS instead of LIND is slightly weaker (-0.35), and slightly less persistent (Fig. 8-b). The LIND-NINO34 correlation at zero lag, based on the multi-model mean, is underestimated by the CMIP5 models and even more by the CMIP3 models (Fig. 8-a). The ISAS-NINO34 correlation at zero lag is realistic in the CMIP5 models, and slightly underestimated in the CMIP3 models (Fig. 8-b). However, the most striking feature of CMIP correlation curves is that they present a very gentle slope the year before the monsoon, as compared to a very steep slope in the observations (Fig. 8-a,b). This is also true after the monsoon season for LIND. We link this bias to the ENSO characteristics in the following paragraph.

In the observations and reanalysis, a positive (negative) anomaly of NINO34 in June-July, i.e. at the beginning of the Indian monsoon, is more related to a developing El Niño (La Niña) event than to a terminating event. Indeed, the correlation between NINO-34 in June-July (beginning of the Indian monsoon) and NINO34 in December prior to the monsoon (December corresponds to the mature stage of ENSO) is only 0.15 (see black curve in Fig. 8-c); by contrast, the correlation between NINO-34 in June-July and NINO34 in December following the monsoon is high (0.80, see Fig. 8-c). This asymmetry is much less marked in the CMIP simulations, in particular in CMIP5, where the equivalent correlation is 0.30 in December before the Indian monsoon, and 0.70 in the following December (green curve in Fig. 8-c). In other words, the June-July NINO34 anomalies are mostly related to developing El Niño or La Niña events in the observations, whereas they are also partly related to the termination of previous-boreal-winter events in CMIP5 (and CMIP3 to a lower extent). This can be explained by the too large spread in the seasonal cycle of NINO34 (and ENSO in general) in the CMIP5 simulations, as described by Taschetto et al. (2012). During the second half of the Indian monsoon (August-September), the NINO34 anomalies are good precursors of developing El Niño or La Niña events (that will be mature in the following December) both in the observations and in CMIP models. Indeed, the correlation in Fig. 8-d is near zero in December prior to the monsoon, and 0.90 in the observations/reanalysis and CMIP5 simulations (0.80 for CMIP3) in December after the Indian monsoon. To summarize, as CMIP5 NINO34 June-July anomalies are too strongly related to previous-boreal-winter El Niño or La Niña events, they produce too large negative correlations between the Indian monsoon and the previous-boreal-winter NINO34 (Fig. 8-a,b). This bias is slightly lower in the CMIP3 simulations, but the correlation between the Indian monsoon and the following-boreal-winter NINO34 is better in CMIP5 than in CMIP3 (Fig. 8-a,b), due to the better consistency between boreal-summer NINO34 anomalies and NINO34 anomalies in the following boreal winter (Fig. 8-c,d). We have to note that the discussion here is from the perspective of a periodic ENSO. There have been periods characterized by a string of El Niño Modoki events during the early 1990s (Ashok et al., 2007). Our description does not account for these particular periods, but holds on average.

Results for individual models are shown in Fig. 9. By looking at the symmetry of the negative correlation to each side of August at zero lag, it is possible to assess if a model produces monsoons mostly correlated to previous ENSO events (e.g. miroc3-2-hires, ACCESS-1.3, that sow strong asymmetric blue bar left of the year-0 line), partly correlated to previous ENSO events (e.g. FIO-ESM shows blue bar to either side of the year-0 line), or mostly correlated to developing ENSO events (e.g. HadGEM2-ES shows strong asymmetric blue bar right of the year-0 line).

Australian monsoon-IOD relationship

We next evaluate the relationship between the IOD and Australian rainfall in the various datasets. There is a weak anti-correlation (hardly significant at the 90% level) between the DJF land-based Australian monsoon (LAUS) and the previous SON (September to November) Indian Dipole Mode index (DMI) for both AWAP and GPCC (represented by δ and γ respectively in Fig. 10-a). This correlation is weaker and not significant for the reanalysis. Both CMIP3 and CMIP5 multi-model means indicate that the models, in average, produce an anti-correlation similar to that of AWAP and GPCC (-0.2). However, the spread across models is large. Interestingly, there is a clear relationship between the strength of the previous DMI-monsoon relationship, and the concomitant ENSO-monsoon relationship in CMIP models (correlation of 0.73, see Fig. 10-a). Over the Maritime continent, models and reanalysis produce much stronger IOD-rainfall anti-correlation than with LAUS (Fig. 10-b), and there is also a clear relationship between the strength of the previous DMI-monsoon relationship, and the concomitant ENSO-monsoon relationship in CMIP models (correlation of 0.66). These results are consistent with the ENSO-IOD seasonal phase-locking relationship that has been described in the literature (Annamalai et al., 2005; Behera et al., 2006; Luo et al., 2010). We have also found that most of the CMIP models reproduce an Indian Ocean Basin-wide Warming (IOBW, Lau and Nath, 2003; Chowdary and Gnanaseelan, 2007; Saji et al., 2006; Ashok et al. under preparation 2012). The simulated IOBW-Australian monsoon relationship is very similar to the ENSO-monsoon relationship shown in Fig. 5 (not shown). However, as the IOBW is essentially a forced response to ENSO, it is not possible to separate their relative contribution without specific idealized experiments (e.g. Taschetto et al., 2011).

Model selection

In the previous subsection, we have selected a subset of models that have good overall monsoon skills in the historical period (Tab. 5). We now examine to what extent these specific models can reproduce the relationships to ENSO, in order to improve the model selection. In the previous analysis, it appears that the AMAR-ENSO relationship is the most robust in the observations (the strongest in terms of correlation). It is also an important area in terms of North-South monsoon connection, at least on the biennial scale (Meehl, 1997); further, there is a clear consensus among observations and reanalysis (Fig. 7). On this basis, we first want to reproduce the link between ENSO SST patterns near the climatological warm pool location and the convection over the Maritime Continent, i.e. we choose to exclude all the models below the 99% significance level for the concomitant ENSO-AMAR correlation (i.e. all the models below the horizontal dashed line in Fig. 7). Results are summarized in Tab. 5). Apart from GFDL-CM3, the excluded models suffer from an unrealistic cold anomaly during El Niño events (and vice versa during La Niña) in the Western Pacific. Then, we decide to allow a bias of ± 0.3 in the DJF LAUS-NINO34 anti-correlation, i.e. we keep correlation values between -0.15 (90% significance level) and -0.75 (i.e. between the dashed lines in Fig. 6-a; see also Tab. 5). We also want some relationship between ENSO and the Indian monsoon. Models with insignificant LIND-NINO34 correlation in JJAS at zero lag (Fig. 9) are therefore excluded (Tab. 5). As the spread in the monsoon-IOD relationship is large in both the observations and models, it is difficult to find clear outliers. Therefore, we do not select the models on an IOD-monsoon relationship basis. Doing this, we select 13 models in the 19 previously selected. Twelve of them are from CMIP5.

3.3 Future monsoon projections

Based on the subset of most realistic models, we now analyze the projected change of the Indo-Australian monsoon in the emission scenario rcp8.5 (see section 2.3). We do not analyze the simulations from the gfdl-cm2-0 CMIP3 model since the emission scenarios in CMIP3 were different from the rcp ones. Among the 12 selected CMIP5 models, all but CESM1-FASTCHEM were available for the rcp8.5 scenario at the time of writing, with several ensemble members for six of them (Tab. 5).

The evolution of the monsoon rainfall in the different boxes used in this paper is shown in Fig. 11. We average the indices over 50-year periods to increase the statistical significance. The confidence interval for each period is thus proportional to $s/\sqrt{50\,N}$, where s is the interannual standard deviation and N the number of ensemble members (t-statistics, e.g. Von Storch and Zwiers, 2002). Two 50-year periods are considered significantly different if there is no overlap of the error bars in Fig. 11 (we consider a confidence interval at the 90% level).

Only two of the 11 models show a significant increase in monsoon rainfall over Australia during the historical period (MIROC5 and FGOALS-s2, Fig. 11-a). This contrasts with the results from Shi et al. (2008) and Smith (2004) who have reported an increase of the observed land-based Australian monsoon rainfall in the 20$^{\text{th}}$century. Now considering the future projections, we find that nine of the 11 CMIP5 models show a significant rainfall increase at the end of the 21$^{\text{st}}$century as compared to the pre-industrial period. This increase is in the range 12-22%. The two remaining model do not show a significant trend from 1850 to 2100.

None of the selected CMIP5 models shows an increase in monsoon rainfall over the

Maritime Continent during the historical period (Fig. 11-b), but one model (HadGEM2-AO) produces less monsoon rainfall at the end of the 20^{th}century than during the pre-industrial period. There is no clear consensus between the models concerning the future monsoon rainfall over the Maritime Continent: three models produce less rainfall in 2050-2099 than during the pre-industrial period (FGOALS-s2, HadGEM2-AO, CanESM2); two models show trends that are not significant at the 90% level (ACCESS1-0 and CESM1-CAM5); the six remaining models produce between 3 and 13% more monsoon rainfall at the end of the 21^{st}century as compared to the end of the 19^{th}century.

The picture is not clear either for the rainfall evolution over India and South-Asia over the historical period (Fig. 11-c,d). Indeed, the majority of models do not show a significant trend, while two models produce slightly more rainfall at the end of the 20^{th}century, and 2-3 models produce less rain during this period. These results must be considered in the perspective of Goswami et al. (2006)'s results: using observations, they have shown that the contribution from increasing heavy events had been offset by decreasing moderate events in the historical period, accounting for an insignificant rainfall trend to date. Contrasting with the absence of model consensus for the historical trend, 10 of the 11 selected models produce significantly more monsoon rainfall at the end of the 21^{st}century than during any of the 50-year historical period. The remaining model (FIO-ESM) does not show any trend. The simulated increase in land-based rainfall ranges from 6 to 18%, except for FGOALS-s2 that produces 46% more rainfall at the end of the 21^{st}century (Fig. 11-c). The increase is in the range 7-15% when considering the whole South Asia domain, except for FGOALS-s2 that produces 27% more monsoon rainfall after 2050 than in the 19^{th}century (Fig. 11-d).

Finally, we investigate potential trends in the amplitude of the interannual variability of the summer monsoon rainfall. This analysis is done in a similar way as for the mean, but using 90% confidence intervals based on the χ^2 statistics (suitable for tests on standard deviations, Von Storch and Zwiers, 2002). Only FGOALS-s2 produces a strengthened interannual variability over Australia (by 45%), the other models producing no significant trend until 2100 (not shown). Over the Maritime Continent (AMAR), four of the 11 selected models show a significant increase of the interannual standard deviation (not shown). Interestingly, two of these models (FGOALS-s2 and HadGEM2-AO) are among the few models that capture a decreased mean AMAR monsoon rainfall at the end of the 21stcentury (as already shown in Fig. 11-b). CCSM4 and FGOALS-s2 produce an increased interannual variability for LIND (by 17 and 60% respectively) and for ISAS (by 20 and 42% respectively), and CESM1-CAM5 produces a significantly increased interannual variability for ISAS (by 25%) but not for LIND (not shown). The remaining models do not show a significant change in the amplitude of the interannual variability.

4 Discussion

In this paper, we have adopted a large-scale point of view, which was needed to assess 60 CMIP models in a concise way. We have found some agreement between the selected models for the Indian and Australian rainfall projections. Nonetheless, the spatial scale of concern for human activities is much narrower than the large-scale used in this paper. Therefore, we now assess the meaning, in term of regional climate, of the future increase in the large-scale precipitation. Historical summer monsoon rainfall and its change in the rcp8.5 scenario are shown on maps, in Fig. 12 and Fig. 13 for the Australian/Maritime Continent region and the Indian monsoon respectively. As already seen in Fig. 11, a majority of the models produce more monsoon rainfall over North Australia in the future. Shi et al. (2008) have reported a larger rainfall increase in North-West Australia than in North-East Australia during the end of the 20$^{\mathrm{th}}$century. There is however no such consensus in the selected rcp8.5 simulations, some of them showing an East-West symmetry in the increase, or the opposite asymmetry (Fig. 12-c).

In Austral summer, the Maritime Continent is at the intersection of three major convergence zones: the South Pacific Convergence Zone (SPCZ), the North Pacific Intertropical Convergence Zone (ITCZ), and the South Indian Convergence Zone (SICZ), their location being shown in Fig. 12-a. As such, the projections of monsoon rainfall over the Maritime Continent are probably sensitive to the evolution of these convergence zones. First, it should be noticed that some models tend to produce too much rainfall in the Western end of the ITCZ as compared to the Western end of the SPCZ during the historical period (e.g. CCSM4, FIO-ESM, MIROC5, NorESM-ME, in Fig. 12-b). Then, the striking thing is that the pattern of projected DJFM rainfall in these convergence zones is totally different from one model to another (Fig. 12-c). Moreover, the Maritime Continent is characterized by marked land-ocean heterogeneities, and by high and narrow mountain ranges, with the Central Range of Papua-New Guinea peaking at 4884 m, and with mountain ranges peaking between 1000 and 3000 m in most of the Indonesian and Malaysian islands. It is worth mentioning that these heterogeneities lead to a very strong uncertainty in any of the observational products. Most of the selected models capture strong monsoon precipitation in Papua-New Guinea, and a few of them capture relatively realistic island-related patterns in Indonesia and Malaysia (CESM1-CAM5, ACCESS1-0, HadGEM2-AO in Fig. 12-b). While most of the models produce an increase of precipitation in Papua-New Guinea during the 21$^{\mathrm{st}}$century, there is no clear consensus across the selected models on the evolution of Indonesian and Malaysian DJFM monsoon rainfall (Fig. 12-c).

As shown in section 3.3, 10 of the 11 selected models produce more summer monsoon rainfall in India and South Asia during the 21stcentury compared to the historical period. There are three regional spots that appear particularly intense in the observations (Fig. 13-a): the Western Ghats (South-Western part of the Indian peninsula), the Eastern coast of the Bay of Bengal, and the Eastern third of the Himalaya. The majority of the selected models simulate such spots in the historical simulations, but tend to produce much stronger rainfall than observed in the Central part of the Himalaya (Fig. 13-b). It should be noted, however, that the uncertainty in both satellite and station-based observations is very high in this region of complex orography. Interestingly, all the models that produce more land-based rainfall in the rcp8.5 scenario have most of the rainfall increase located in the Himalaya (Fig. 13-c). There is however no consensus across the selected models on how the summer monsoon rainfall could vary along the Eastern coast of the Bay of Bengal. Approximately half of the models produce slightly less rainfall in the Western Ghats during the 21stcentury (e.g. MIROC5, HadGEM2-AO, CESM1-CAM5), in qualitative agreement with Rajendran et al. (2012) who obtained such results from a high resolution atmospheric model.

5 Conclusion

In this paper, we have shown that a critical challenge in model rainfall assessment lies in the spread of observational data. Indeed, the mean summer monsoon rainfall and the amplitude of its interannual variability vary significantly across the observation datasets. The atmospheric reanalysis produce monsoon rainfall in the range of the observations uncertainty.

By building an envelope of the observations and reanalysis, it is possible to identify the outliers, i.e. the models that are significantly different from the observations. Most of the CMIP3 and CMIP5 models produce both Indian and Australian mean summer monsoon rainfall reasonably close to the observations/reanalysis envelope. This is also true for the amplitude of the interannual variability of the Indian and Australian summer monsoons. The seasonal cycle of both the Indian and the Australian monsoons is in good agreement across the observation products and reanalysis. Most of the CMIP3 and CMIP5 models capture a seasonal cycle with a maximum rainfall at the right season, but the seasonal cycle tends to be shorter or longer than observed in the CMIP5 simulations, and even more in the CMIP3 simulations. Based on the mean monsoon rainfall, on the amplitude of its interannual variability, and on the seasonal cycle, we select a subset of 19 models that statistically capture the main characteristics of the monsoon, taking the observations uncertainty into account.

Then, we have evaluated the monsoon-ENSO and monsoon-IOD relationships in the CMIP models, because ENSO and IOD are likely to change in a future climate, with possible consequences for the monsoon. Because of their difference in seasonality, the Australian/Maritime Continent monsoon-ENSO relationship and the Indian/South Asian monsoon-ENSO relationship are affected by different kinds of biases in the CMIP models. As already noted in previous studies related to the CMIP3 models, we have confirmed that the intensity of the concomitant land-based Australian monsoon-ENSO relationship is correlated to the intensity of simulated ENSO (this had already been noted by Cai et al., 2009 and Colman et al., 2011 for the CMIP3 models). We have shown that the monsoon-ENSO relationship over the Maritime continent is rather influenced by the ability of the models to produce a cold anomaly in the climatological warm pool during El Niño events. In India and South Asia, the monsoon-ENSO relationship strongly depends on the simulated seasonal cycle of ENSO, because El Niño or La Niña events are at their developing stage at the beginning of the monsoon (whereas the Australian monsoon co-occurs with ENSO at its mature stage). As the ENSO seasonal cycle is longer than observed in the CMIP simulations (Taschetto et al., 2012), the CMIP models tend to produce monsoon rainfall that is too much influenced by the tails of ENSO events from the previous year. The SON IOD generally influences the monsoon rainfall over the Maritime Continent in the CMIP3 and the CMIP5 simulations, and to a lesser extent over Australia. The strength of the monsoon-IOD link in the models is correlated to the strength of the monsoon-ENSO link.

Based on these findings, we have empirically chosen a few criteria to refine the model selection, towards models that do not present major biases with regards to the monsoon-ENSO relationship. We end up with 13 models that represent the statistical properties of the Indian and Australian monsoon well and have also relatively good skills in simulating ENSO-monsoon relationship. Twelve of these 13 models are from CMIP5. We have then analyzed the change of monsoon rainfall in the rcp8.5 emission scenario for the 11 available CMIP5 models. A large majority of these 11 models produce significantly more summer monsoon rainfall in India (10/11), in the South Asia region (10/11), and in Australia (9/11) at the end of the 21stcentury. Thus, the models generally produce 5 to 20% more summer monsoon rainfall in 2050-2099 as compared to the pre-industrial period (and much more in the FGOALS-s2 model). In India, most of the simulated increase takes place in the Himalaya. By contrast, only five of the 11 models produce significantly more monsoon rainfall over the Maritime Continent at the end of the 21stcentury. Two models (FGOALS-s2 and HadGEM2-AO) project slightly less monsoon rainfall over the Maritime Continent in the future, but associated with a strengthened interannual variability. For the majority of the models, there is no significant change in the amplitude of the interannual monsoon rainfall variability. Considering maps of projected rainfall patterns, we find no consistency between the selected models over the Maritime Continent.

Our concluding remark is that the best CMIP5 models have stronger skills than the best CMIP3 models, but the best models are still unable to resolve the complexity of the Maritime Continent. This leads to the absence of model consensus concerning the future monsoon rainfall in this region. It is likely that high-resolution modeling is needed to simulate the climate of this region, due to complex land/sea distribution and to complex orography and bathymetry.

Acknowledgment

This study was conducted in the context of the ARC project DP110100601. KA received supports from IITM and MoES-NERC. We acknowledge the World Climate Research Programme's Working Group on Coupled Modelling, which is responsible for CMIP, and we thank the climate modeling groups (Tab. 3, 4) for producing and making available their model output. The U.S. Department of Energy's Program for Climate Model Diagnosis and Intercomparison (PCMDI) provided coordinating support and led development of software infrastructure in partnership with the Global Organization for Earth System Science Portals. We thank the Australian National Computational Infrastructure (NCI) for help in the download process. We acknowledge all the Institutions in Tab. 2 for having made their observations and reanalysis accessible to us.

References

Adler, R., Huffman, G., Chang, A., Ferraro, R., Xie, P., Janowiak, J., Rudolf, B., Schneider, U., Curtis, S., Bolvin, D., et al. (2003). The version 2 global precipitation climatology project (GPCP) monthly precipitation analysis (1979-present). *Journal of Hydrometeorology*, 4(6):1147–1167.

Adler, R. F., Huffman, G. J., Bolvin, D. T., Curtis, S., and Nelkin, E. J. (2000). Tropical rainfall distributions determined using TRMM combined with other satellite and rain gauge information. *J. Appl. Meteorol.*, 39(12):2007–2023.

Annamalai, H., Xie, S. P., McCreary, J. P., and Murtugudde, R. (2005). Impact of Indian Ocean Sea Surface Temperature on Developing El Niño. *J. Climate*, 18(2):302–319.

Ashok, K., Behera, S. K., Rao, S. A., Weng, H., and Yamagata, T. (2007). El Niño Modoki and its possible teleconnection. *J. Geophys. Res*, 112(10.1029).

Ashok, K., Guan, Z., and Yamagata, T. (2001). Impact of the Indian Ocean dipole on the relationship between the Indian monsoon rainfall and ENSO. *Geophys. Res. Lett.*, 28(23):4499–4502.

Behera, S. K., Luo, J. J., Masson, S., Rao, S. A., Sakuma, H., and Yamagata, T. (2006). A CGCM study on the interaction between IOD and ENSO. *J. Climate*, 19(9):1688–1705.

BOM (2010). Operational implementation of the ACCESS numerical weather prediction system. NMOC Operations Bulletin No.83. Technical report, Bureau of Meteorology (BOM).

Boos, W. R. and Kuang, Z. (2010). Dominant control of the South Asian monsoon by orographic insulation versus plateau heating. *Nature*, 463(7278):218–222.

Bosilovich, M. G., Chen, J., Robertson, F. R., and Adler, R. F. (2008). Evaluation of global precipitation in reanalyses. *J. Appl. Meteorol. and Climatology*, 47(9):2279–2299.

Cai, W., Hendon, H. H., and Meyers, G. (2005). Rainfall Teleconnections with Indo-Pacific Variability in the WCRP CMIP3 Models. *J. Climate*, 18:1449–1468.

Cai, W., Sullivan, A., and Cowan, T. (2009). Rainfall Teleconnections with Indo-Pacific Variability in the WCRP CMIP3 Models. *J. Climate*, 22:5046–5070.

Catto, J. L., Nicholls, N., and Jakob, C. (2012). North Australian sea surface temperatures and the El Niño Southern Oscillation in observations and models. *J. Climate*.

Chao, W. and Chen, B. (2001). The origin of monsoons. *J. Atmos. Sci.*, 58(22):3497–3507.

Chowdary, J. S. and Gnanaseelan, C. (2007). Basin-wide warming of the Indian Ocean during El Niño and Indian Ocean dipole years. *Int. J. Climatol.*, 27(11):1421–1438.

Chung, C. and Ramanathan, V. (2006). Weakening of North Indian SST gradients and the monsoon rainfall in India and the Sahel. *J. Climate*, 19(10):2036–2045.

Collins, M., Tett, S., and Cooper, C. (2001). The internal climate variability of HadCM3, a version of the Hadley Centre coupled model without flux adjustments. *Clim. Dynam.*, 17(1):61–81.

Collins, W., Bellouin, N., Doutriaux-Boucher, M., Gedney, N., Halloran, P., Hinton, T., Hughes, J., Jones, C., Joshi, M., Liddicoat, S., et al. (2011). Development and evaluation of an Earth-system model–HadGEM2. *Geosci. Model Dev. Discuss*, 4:997–1062.

Collins, W., Bitz, C., Blackmon, M., Bonan, G., Bretherton, C., Carton, J., Chang, P., Doney, S., Hack, J., Henderson, T., et al. (2006). The community climate system model version 3 (CCSM3). *J. Climate*, 19(11):2122–2143.

Colman, R. A., Moise, A. F., and Hanson, L. I. (2011). Tropical Australian climate and the Australian monsoon as simulated by 23 CMIP3 models. *J. Geophys. Res.*, 116(D10):D10116.

Dee, D. P., Uppala, S. M., Simmons, A. J., Berrisford, P., Poli, P., Kobayashi, S., Andrae, U., et al. (2011). The ERA-Interim reanalysis: Configuration and performance of the data assimilation system. *Q. J. Roy. Meteorol. Soc.*, 137(656):553–597.

Delworth, T., Broccoli, A., Rosati, A., Stouffer, R., Balaji, V., Beesley, J., Cooke, W., et al. (2006). GFDL's CM2 global coupled climate models. Part I: Formulation and simulation characteristics. *J. Climate*, 19(5):643–674.

Donner, L. J., Wyman, B. L., Hemler, R. S., Horowitz, L. W., Ming, Y., Zhao, M., Golaz, J. C., et al. (2011). The Dynamical Core, Physical Parameterizations, and Basic Simulation Characteristics of the Atmospheric Component AM3 of the GFDL Global Coupled Model CM3. *J. Climate*, 24(13):3484–3519.

Dufresne, J.-L., Foujols, M.-A., Denvil, S., Caubel, A., Marti, O., Aumont, O., Balkanski, Y., et al. (2012). Climate change projections using the IPSL-CM5 Earth System Model: from CMIP3 to CMIP5. *submitted to Clim. Dynam.*

Furevik, T., Bentsen, M., Drange, H., Kindem, I. K. T., Kvamstø, N. G., and Sorteberg, A. (2003). Description and evaluation of the Bergen climate model: ARPEGE coupled with MICOM. *Clim. Dynam.*, 21(1):27–51.

Gent, P. R., Danabasoglu, G., Donner, L. J., Holland, M. M., Hunke, E. C., Jayne, S. R., Lawrence, D. M., et al. (2011). The Community Climate System Model Version 4. *J. Climate*, 24:4973–4991.

Gordon, C., Cooper, C., Senior, C. A., Banks, H., Gregory, J. M., Johns, T. C., Mitchell, J. F. B., and Wood, R. A. (2000). The simulation of SST, sea ice extents and ocean heat transports in a version of the Hadley Centre coupled model without flux adjustments. *Clim. Dynam.*, 16(2):147–168.

Gordon, H. B., Rotstayn, L. D., McGregor, J. L., Dix, M. R., Kowalczyk, E. A., and O'Farrell, S. P. (2002). The CSIRO Mk3 Climate System Model, CSIRO Atmospheric Research technical paper No. 60. Technical report, Commonwealth Scientific and Industrial Research Organisation, Australia.

Goswami, B. N., Venugopal, V., Sengupta, D., Madhusoodanan, M. S., and Xavier, P. K. (2006). Increasing trend of extreme rain events over India in a warming environment. *Science*, 314(5804):1442–1445.

Gualdi, S., Scoccimarro, E., and Navarra, A. (2008). Changes in Tropical Cyclone Activity due to Global Warming: Results from a High-Resolution Coupled General Circulation Model. *J. Climate*, 21(20):5204–5228.

Hazeleger, W., Severijns, C., Semmler, T., Éireann, M., Ştefănescu, S., Yang, S., Wang, X., Wyser, K., and Dutra, E. (2010). EC-Earth: a seamless earth system prediction approach in action. *Bull. Amer. Meteor. Soc*, 91:1357–1363.

Holland, G. J. (1986). Interannual variability of the Australian summer monsoon at Darwin: 1952-82. *Mon. Wea. Rev.*, 114(3):594–604.

Izumo, T., Montégut, C., Luo, J., Behera, S., Masson, S., and Yamagata, T. (2008). The role of the western Arabian Sea upwelling in Indian monsoon rainfall variability. *J. Climate*, 21(21):5603–5623.

Johns, T., Durman, C., Banks, H., Roberts, M., McLaren, A., Ridley, J., Senior, C., Williams, K., Jones, A., Keen, A., et al. (2004). HadGEM1–Model description and analysis of preliminary experiments for the IPCC Fourth Assessment Report. *Hadley Centre Technical Note*, 55.

Jones, D., Wang, W., and Fawcett, R. (2009). High-quality spatial climate data-sets for Australia. *Australian Meteorological and Oceanographic Journal*, 58(4):233.

Jungclaus, J. H., Keenlyside, N., Botzet, M., Haak, H., Luo, J. J., Latif, M., Marotzke, J., Mikolajewicz, U., and Roeckner, E. (2006). Ocean circulation and tropical variability in the coupled model ECHAM5/MPI-OM. *J. Climate*, 19(16):3952–3972.

K-1 model developers (2004). K-1 coupled model (MIROC) description, Tech. Rep. 1. Technical report, Center for Climate System Research, University of Tokyo.

Kalnay, E., Kanamitsu, M., Kistler, R., Collins, W., Deaven, D., Gandin, L., Iredell, M., Saha, S., White, G., Woollen, J., et al. (1996). The NCEP/NCAR 40-Year Reanalysis Project. *Bull. Am. Meteorol. Soc.*, 77:437–472.

Kim, S. J., Flato, G., Boer, G., and McFarlane, N. (2002). A coupled climate model simulation of the Last Glacial Maximum, Part 1: transient multi-decadal response. *Clim. Dynam.*, 19(5):515–537.

Kim, S. T. and Yu, J.-Y. (2012). The two types of ENSO in CMIP5 models. *Geophys. Res. Lett., 39, L11704*, 39:L11704.

Krishnan, R., Sabin, T. P., Ayantika, D. C., Kitoh, A., Sugi, M., Murakami, H., Turner, A. G., Slingo, J. M., and Rajendran, K. (2012). Will the South Asian monsoon overturning circulation stabilize any further? *Clim. Dynam., in press.*

Kumar, K. K., Rajagopalan, B., Hoerling, M., Bates, G., and Cane, M. (2006). Unraveling the mystery of Indian monsoon failure during El Nino. *Science*, 314(5796):115–119.

Lau, N. C. and Nath, M. J. (2003). Atmosphere-ocean variations in the Indo-Pacific sector during ENSO episodes. *J. Climate*, 16(1):3–20.

Li, Y., Jourdain, N. C., Taschetto, A. S., Ummenhofer, C. C., Ashok, K., and Sen Gupta, A. (2012). Evaluation of Monsoon Fidelity and the Tropospheric Biennial Oscillation Transitions in the CMIP Models. *Submitted to Geophys. Res. Lett.*

Liu, X. and Yanai, M. (2001). Relationship between the Indian monsoon rainfall and the tropospheric temperature over the Eurasian continent. *Q. J. Roy. Meteorol. Soc.*, 127(573):909–937.

Lucarini, V. and Russell, G. L. (2002). Comparison of mean climate trends in the northern hemisphere between National Centers for Environmental Prediction and two atmosphere-ocean model forced runs. *J. Geophys. Res*, 107(10.1029).

Luo, J. J., Zhang, R., Behera, S. K., Masumoto, Y., Jin, F. F., Lukas, R., and Yamagata, T. (2010). Interaction between El Nino and extreme Indian ocean dipole. *J. Climate*, 23(3):726–742.

Marti, O., Braconnot, P., Bellier, J., Benshila, R., Bony, S., Brockmann, P., Cadule, P., et al. (2005). The new IPSL climate system model: IPSL-CM4, Note du Pôle de Modélisation, IPSL 26. Technical report, Institut Pierre Simon Laplace, France.

Martin, G. M., Bellouin, N., Collins, W. J., Culverwell, I. D., Halloran, P. R., Hardiman, S. C., Hinton, T. J., et al. (2011). The HadGEM2 family of Met Office Unified Model Climate configurations. *Geosci. Model Dev. Discuss.*, 4:765–841.

Meehl, G. A. (1997). The south Asian monsoon and the tropospheric biennial oscillation. *J. Climate*, 10(8):1921–1943.

Meehl, G. A. and Arblaster, J. M. (2002). The tropospheric biennial oscillation and Asian-Australian monsoon rainfall. *J. Climate*, 15(7):722–744.

Meehl, G. A., Stocker, T. F., Collins, W., Friedlingstein, P., Gaye, A., Gregory, J., et al. (2007). Chapter 10: Global Climate Projections. In: Climate Change 2007: The Physical Science Basis. Contribution of Working Group I to the Fourth Assessment Report of the Intergovernmental Panel on Climate Change.

Min, S. K. and Hense, A. (2006). A Bayesian assessment of climate change using multimodel ensembles. Part I: Global mean surface temperature. *J. Climate*, 19(13):3237–3256.

Mishra, V., Smoliak, B. V., Lettenmaier, D. P., and Wallace, J. M. (2012). A prominent pattern of year-to-year variability in Indian Summer Monsoon Rainfall. *Proceedings of the National Academy of Sciences.*

Moise, A. F., Colman, R. A., and Brown, J. R. (2012). Behind uncertainties in projections of Australian tropical climate: Analysis of 19 CMIP3 models. *J. Geophys. Res.*, 117(D10):D10103.

Moss, R. H., Edmonds, J. A., Hibbard, K. A., Manning, M. R., Rose, S. K., van Vuuren, D. P., Carter, T. R., et al. (2010). The next generation of scenarios for climate change research and assessment. *Nature*, 463(7282):747–756.

Neale, R. and Slingo, J. (2003). The maritime continent and its role in the global climate: A GCM study. *J. Climate*, 16(5):834–848.

Onogi, K., Tsutsui, J., Koide, H., Sakamato, M., Kobayashi, S., Hatsushika, H., Matsumoto, T., et al. (2007). The JRA-25 Reanalysis. *J. Meteorol. Soc. Japan*, 85(3):369–432.

Raddatz, T., Reick, C., Knorr, W., Kattge, J., Roeckner, E., Schnur, R., Schnitzler, K., Wetzel, P., and Jungclaus, J. (2007). Will the tropical land biosphere dominate the climate–carbon cycle feedback during the twenty-first century? *Clim. Dynam.*, 29(6):565–574.

Rajendran, K., Kitoh, A., Srinivasan, J., Mizuta, R., and Krishnan, R. (2012). Monsoon circulation interaction with Western Ghats orography under changing climate. *Theoretical and Applied Climatology*, pages 1–17.

Randall, D. A., Wood, R. A., Bony, S., Colman, R., Fichefet, T., Fyfe, J., Kattsov, V., et al. (2007). *Cilmate Models and Their Evaluation. In: Climate Change 2007: The Physical Science Basis. Contribution of Working Group I to the Fourth Assessment Report of the Intergovernmental Panel on Climate Change.* Cambridge University Press, Cambridge, United Kingdom and New York, NY, USA.

Rayner, N. A., Brohan, P., Parker, D. E., Folland, C. K., Kennedy, J. J., Vanicek, M., Ansell, T. J., and Tett, S. F. B. (2006). Improved analyses of changes and uncertainties in sea surface temperature measured in situ since the mid-nineteenth century: The HadSST2 dataset. *J. Climate*, 19(3):446–469.

Rayner, N. A., Parker, D. E., Horton, E. B., Folland, C. K., Alexander, L. V., Rowell, D. P., Kent, E. C., and Kaplan, A. (2003). Global analyses of sea surface temperature, sea ice, and night marine air temperature since the late nineteenth century. *J. Geophys. Res*, 108(D14):4407.

Riahi, K., Rao, S., Krey, V., Cho, C., Chirkov, V., Fischer, G., Kindermann, G., Nakicenovic, N., and Rafaj, P. (2011). RCP 8.5 A scenario of comparatively high greenhouse gas emissions. *Climatic change*, pages 1–25.

Rienecker, M. M., Suarez, M. J., Gelaro, R., Todling, R., Bacmeister, J., Liu, E., Bosilovich, M. G., et al. (2011). MERRA: NASA's Modern-Era Retrospective Analysis for Research and Applications. *J. Climate*, 24(14):3624–3648.

Rotstayn, L. D., Collier, M. A., Dix, M. R., Feng, Y., Gordon, H. B., O'Farrell, S. P., Smith, I. N., and Syktus, J. (2010). Improved simulation of Australian climate and ENSO-related rainfall variability in a global climate model with an interactive aerosol treatment. *Int. J. Climatol.*, 30(7):1067–1088.

Rotstayn, L. D., Jeffrey, S. J., Collier, M. A., Dravitzki, S. M., Hirst, A. C., Syktus, J. I., and Wong, K. K. (2012). Aerosol-induced changes in summer rainfall and circulation in the Australasian region: a study using single-forcing climate simulations. *Atmos. Chem. Phys. Discuss*, 12:6377–6404.

Roxy, M., Patil, N., and Ashok, K. (2012). Indian summer monsoon-ENSO links in the IPCC AR4 projections: A cautionary outlook. *Submitted to Global and Planetary Change*.

Rudolf, B., Becker, A., Schneider, U., Meyer-Christoffer, A., and Ziese, M. (2011). New GPCC Full Data Reanalysis Version 5 Provides High-Quality Gridded Monthly Precipitation Data. Technical report, Global Precipitation Climatology Centre, Offenbach, Germany.

Saha, S., Moorthi, S., Pan, H., Wu, X., Wang, J., Nadiga, S., Tripp, P., et al. (2010). The NCEP climate forecast system reanalysis. *Bull. Am. Meteorol. Soc.*, 91(8):1015–1057.

Saji, N. H., Goswami, B. N., Vinayachandran, P. N., and Yamagata, T. (1999). A dipole mode in the tropical Indian Ocean. *Nature*, 401(6751):360–363.

Saji, N. H., Xie, S. P., and Yamagata, T. (2006). Tropical Indian Ocean Variability in the IPCC Twentieth-Century Climate Simulations. *J. Climate*, 19(17):4397–4417.

Saji, N. H. and Yamagata, T. (2003). Possible impacts of Indian Ocean dipole mode events on global climate. *Climate Res.*, 25(2):151–169.

Salas-Mélia, D., Chauvin, F., Déqué, M., Douville, H., Gueremy, J., Marquet, P., Planton, S., Royer, J. F., and Tyteca, S. (2005). Description and validation of the CNRM-CM3 global coupled model, Note 103. Technical report, Centre National de Recherche Météorologique.

Schmidt, G. A., Ruedy, R., Hansen, J. E., Aleinov, I., Bell, N., Bauer, M., Bauer, S., Cairns, B., Canuto, V., Cheng, Y., et al. (2006). Present-day atmospheric simulations using GISS ModelE: Comparison to in situ, satellite, and reanalysis data. *J. Climate*, 19(2):153–192.

Scoccimarro, E., Gualdi, S., Bellucci, A., Sanna, A., Giuseppe Fogli, P., Manzini, E., Vichi, M., Oddo, P., and Navarra, A. (2011). Effects of Tropical Cyclones on Ocean Heat Transport in a High-Resolution Coupled General Circulation Model. *J. Climate*, 24(16):4368–4384.

Shi, G., Cai, W., Cowan, T., Ribbe, J., Rotstayn, L., and Dix, M. (2008). Variability and trend of North West Australia rainfall: observations and coupled climate modeling. *J. Climate*, 21(12):2938–2959.

Smith, I. (2004). An assessment of recent trends in Australian rainfall. *Aust. Meteorol. Mag.*, 53(3):163–173.

Smith, I. N., Moise, A. F., and Colman, R. A. (2012). Large-scale circulation features in the tropical western Pacific and their representation in climate models. *J. Geophys. Res.*, 117(D4):D04109.

Taschetto, A. S. and England, M. H. (2009). El Nino Modoki impacts on Australian rainfall. *J. Climate*, 22(11):3167–3174.

Taschetto, A. S., Sen Gupta, A., Hendon, H. H., Ummenhofer, C. C., and England, M. H. (2011). The Contribution of Indian Ocean Sea Surface Temperature Anomalies on Australian Summer Rainfall during El Niño Events. *J. Climate*, 24:3734–3747.

Taschetto, A. S., Sen Gupta, A., Jourdain, N. C., Agus Santoso, A., Ummenhofer, C. C., and England, M. H. (2012). Cold tongue and warm pool ENSO events in CMIP5: mean state and future projections. *Submitted to J. Climate.*

Taschetto, A. S., Ummenhofer, C. C., Gupta, A. S., and England, M. H. (2009). Effect of anomalous warming in the central Pacific on the Australian monsoon. *Geophys. Res. Lett*, 36(5):L12704.

Taylor, K. E. (2001). Summarizing multiple aspects of model performance in a single diagram. *J. Geophys. Res*, 106(D7):7183–7192.

Taylor, K. E., Stouffer, R. J., and Meehl, G. A. (2011). An overview of CMIP5 and the experiment design. *Bull. Am. Meteorol. Soc.*

Ummenhofer, C. C., Sen Gupta, A., Li, Y., Taschetto, A. S., and England, M. H. (2011). Multi-decadal modulation of the El Nino–Indian monsoon relationship by Indian Ocean variability. *Environ. Res. Lett.*, 6:034006.

Vertenstein, M., Craig, T., Middleton, A., Feddema, D., and Fischer, C. (2012). CESM-1.0.4 User's Guide. Technical report, Community Earth System Model, NCAR, USA.

Voldoire, A., Sanchez-Gomez, E., y Mélia, D., Decharme, B., Cassou, C., Sénési, S., Valcke, S., Beau, I., Alias, A., Chevallier, M., et al. (2012). The CNRM-CM5. 1 global climate model: Description and basic evaluation. *Clim. Dynam. published online.*

Volodin, E. M., Dianskii, N. A., and Gusev, A. V. (2010). Simulating present-day climate with the INMCM4. 0 coupled model of the atmospheric and oceanic general circulations. *Izvestiya Atmospheric and Oceanic Physics*, 46(4):414–431.

Volodin, E. M. and Diansky, N. A. (2004). El-Niño reproduction in coupled general circulation model of atmosphere and ocean. *Russ. Meteorol. Hydrol.*, 12:5–14.

Von Storch, H. and Zwiers, F. (2002). *Statistical analysis in climate research.* Cambridge Univ Pr.

Washington, W. M., Weatherly, J. W., Meehl, G. A., Semtner Jr, A. J., Bettge, T. W., Craig, A. P., Strand Jr, W. G., et al. (2000). Parallel climate model (PCM) control and transient simulations. *Clim. Dynam.*, 16(10):755–774.

Watanabe, M., Suzuki, T., O'ishi, R., Komuro, Y., Watanabe, S., Emori, S., Takemura, T., Chikira, M., Ogura, T., Sekiguchi, M., et al. (2010). Improved Climate Simulation by MIROC5: Mean States, Variability, and Climate Sensitivity. *J. Climate*, 23(23):6312–6335.

Watanabe, S., Hajima, T., Sudo, K., Nagashima, T., Takemura, T., Okajima, H., Nozawa, T., Kawase, H., Abe, M., Yokohata, T., et al. (2011). MIROC-ESM: model description and basic results of CMIP5-20c3m experiments. *Geosci. Model Dev. Discuss.*, 4:1063–1128.

Wittenberg, A. T. (2009). Are historical records sufficient to constrain ENSO simulations. *Geophys. Res. Lett*, 36:L12702.

Xie, P. and Arkin, P. A. (1997). Global precipitation: A 17-year monthly analysis based on gauge observations, satellite estimates, and numerical model outputs. *Bull. Am. Meteorol. Soc.*, 78(11):2539–2558.

Yano, J. I. and McBride, J. L. (1998). An aquaplanet monsoon. *J. Atmos. Sci.*, 55(8):1373–1399.

Yatagai, A., Kamiguchi, K., Arakawa, O., Hamada, A., Yasutomi, N., and Kitoh, A. (2012). APHRODITE: Constructing a long-term daily gridded precipitation dataset for Asia based on a dense network of rain gauges. *Bulletin of American Meteorological Society*.

Yin, X., Gruber, A., and Arkin, P. (2004). Comparison of the GPCP and CMAP merged gauge-satellite monthly precipitation products for the period 1979-2001. *Journal of Hydrometeorology*, 5(6):1207–1222.

Yongqiang, Y., Xuehong, Z., and Yufu, G. (2004). Global coupled ocean-atmosphere general circulation models in LASG/IAP. *Advances in Atmospheric sciences*, 21(3):444–455.

Yu, J. Y. and Kim, S. T. (2010). Identification of Central-Pacific and Eastern-Pacific types of ENSO in CMIP3 models. *Geophys. Res. Lett*, 37:L15705.

Yukimoto, S., Noda, A., Kitoh, A., Sugi, M., Kitamura, Y., Hosaka, M., Shibata, K., Maeda, S., and Uchiyama, T. (2001). The new Meteorological Research Institute coupled GCM(MRI-CGCM 2)- Model climate and variability. *Papers in Meteorology and Geophysics*, 51(2):47–88.

Index	Long name	Var.	References
LIND	land-only Indian monsoon	precip	
ISAS	South Asia / Indian monsoon	precip	Meehl and Arblaster, 2002
LAUS	land-only Australian monsoon	precip	
AMAR	Maritime Continent / Australian monsoon	precip	Meehl and Arblaster, 2002
NINO34	ENSO central index	SST	
DMI	(Indian) Dipole Mode Index	SST	Saji and Yamagata, 2003
IOBW	Indian Ocean Basin Wide Warming index	SST	Taschetto et al., 2011

Table 1: Indices used in this paper (see Fig. 1).

Acronym	ID	Institute	Spatial coverage	Start date	Resol	References
CMAP	α	UCAR/NCAR/CISL/DSS	Global	1979	2.5°	Xie and Arkin, 1997
GPCP	β	NOAA/OAR/ESRL PSD,	Global	1979	2.5°	Adler et al., 2003
GPCC	γ	Boulder, CO, USA	Global land	1901	0.5°	Rudolf et al., 2011
AWAP	δ	BOM, Australia	Austr. land	1900	0.25°	Jones et al., 2009
APHRODITE	δ	ERTDF, Japan	S-E Asia land	1951	0.25°	Yatagai et al., 2012
TRMM-3B42 v6	ϵ	NASA/GIES/DISC,	50°S -50°N	1998	0.25°	Adler et al., 2000
TRMM-3B43 v6	ζ	USA	50°S -50°N	1998	0.25°	Adler et al., 2000
HadISST	η	Met Office,	Global	1870	1.0°	Rayner et al., 2003
HadSST2	θ	Hadley Centre, UK	Global	1850	5.0°	Rayner et al., 2006
NCEP-NCAR I	λ	NOAA/OAR/ESRL PSD,	Global	1948	2.5°	Kalnay et al., 1996
NCEP-DOE II	μ	Boulder, CO,	Global	1979	2.5°	Kalnay et al., 1996
NCEP-CFSR	π	USA	Global	1979	0.5°	Saha et al., 2010
ERA-40	ρ	ECMWF, UK	Global	1957	2.5°	Dee et al., 2011
ERAinterim	τ	ECMWF, UK	Global	1979	0.7°	Dee et al., 2011
JRA-25	ψ	JMA/CRIEPI, Japan	Global	1979	2.5°	Onogi et al., 2007
MERRA	σ	NASA	Global	1979	0.5°	Rienecker et al., 2011

Table 2: Observations (precipitation in upper part, SST in the middle part) and atmospheric reanalysis (lower part) used in this paper. If "land" is not mentioned, precipitation datasets cover both land and ocean. Most of the datasets cover up to the recent years (around 2010), except ERA40 that was stopped in 2002 and APHRODITE that is only available until 2007. The resolution mentioned here is the one of the gridded dataset, even if most of the reanalysis are produced using spectral models.

Model	I D	Institute	Ocean horizontal resolution	Atmos. horiz. resol.	Ens O/A	References
bccr-bcm2-0	a	BCCR, Norway	1.0×1.0 (1.0)	2.8×2.8	1/1	Furevik et al., 2003
cccma-cgcm3-1	b	CCCMA, BC,	1.9×1.9 (1.9)	3.7×3.7	2/5	Kim et al., 2002
cccma-cgcm3-1-t63	c	Canada	1.4×0.9 (0.9)	2.8×2.8	1/1	Kim et al., 2002
cnrm-cm3	d	CNRM, France	2.0×1.0 (1.0)	2.8×2.8	1/1	Salas-Mélia et al., 2005
csiro-mk3-0	e	CSIRO,	1.9×0.9 (0.9)	1.9×1.9	1/2	Gordon et al., 2002
csiro-mk3-5	f	Australia	1.9×0.9 (0.9)	1.9×1.9	1/1	Gordon et al., 2002
gfdl-cm2-0	g	NOAA, GFDL,	1.0×1.0 (0.4)	2.5×2.0	1/1	Delworth et al., 2006
gfdl-cm2-1	h	USA	1.0×1.0 (0.4)	2.5×2.0	1/3	Delworth et al., 2006
giss-aom	i	NASA/GISS,	4.0×3.0 (3.0)	4.0×3.0	1/2	Lucarini and Russell, 2002
giss-model-e-h	j	USA	1.0×1.0 (1.0)	5.0×4.0	4/5	Schmidt et al., 2006
giss-model-e-r	k	" " "	5.0×4.0 (4.0)	5.0×4.0	9/9	Schmidt et al., 2006
iap-fgoals1-0-g	l	IAP, China	1.0×1.0 (1.0)	2.8×2.8	3/3	Yongqiang et al., 2004
ingv-echam4	m	INGV, Italy	1.0×1.0 (1.0)	1.1×1.1	1/1	Gualdi et al., 2008
inmcm3-0	n	INM, Russia	2.5×2.0 (2.0)	5.0×4.0	1/1	Volodin and Diansky, 2004
ipsl-cm4	o	IPSL, France	2.0×1.0 (1.0)	3.7×2.5	1/1	Marti et al., 2005
miroc3-2-hires	p	CCSR,	1.2×0.6 (0.6)	1.1×1.1	1/1	K-1 Developers, 2004
miroc3-2-medres	q	Japan	1.4×0.9 (0.6)	2.8×2.8	1/3	K-1 Developers, 2004
miub-echo-g	r	MIUB, Germany & Korea	2.8×2.3 (0.5)	3.7×3.7	2/5	Min and Hense, 2006
mpi-echam5	s	MPI-M, Germany	1.0×1.0 (1.0)	1.9×1.9	1/3	Jungclaus et al., 2006
mri-cgcm2-3-2a	t	MRI, Japan	2.5×2.0 (0.5)	2.8×2.8	5/5	Yukimoto et al., 2001
ncar-ccsm3-0	u	NCAR, CO, USA	1.1×0.5 (0.3)	1.4×1.4	2/8	Collins et al., 2006
ncar-pcm1	v	NCAR, CO, USA	1.0×1.0 (1.0)	2.8×2.8	3/4	Washington et al., 2000
ukmo-hadcm3	w	MOHC, UK	1.2×1.2 (1.2)	3.8×2.5	1/2	Gordon et al., 2000
ukmo-hadgem1	x	MOHC, UK	1.0×1.0 (0.4)	1.9×1.2	1/2	Johns et al., 2004

Table 3: CMIP3 model names; ID for this paper; name of providing institutes; ocean mean zonal resolution (at the equator in °E) × mean 25°N -35°N resolution in latitude (in °), and mean equatorial refinement in brackets (5°S -5°N); atmospheric output resolution (in °E × °N); the number of ensemble members for the Ocean/Atmosphere components is shown in the Ens O/A column.

Model	I D	Institute	Ocean horizontal resolution	Atmos. horiz. resol.	Ens O/A	References
ACCESS-1.0	A	CSIRO-BOM,	1.0×1.0 (0.3)	1.9×1.2	1/1	BOM, 2010
ACCESS-1.3	B	Australia	1.0×1.0 (0.3)	1.9×1.2	1/1	BOM, 2010
BCC-CSM1-1	C	BCC, CMA, China	1.0×1.0 (0.3)	2.8×2.8	3/3	
CanESM2	D	CCCMA, Canada	1.4×0.9 (0.9)	2.8×2.8	5/5	
CESM1-CAM5	E	NSF-DOE-	1.1×0.6 (0.3)	1.2×0.9	2/3	Vertenstein et al., 2012
CESM1-FASTCHEM	F	-NCAR,	1.1×0.6 (0.3)	1.2×0.9	3/3	Vertenstein et al., 2012
CESM1-WACCM	G	USA	1.1×0.6 (0.3)	2.5×1.9	1/1	Vertenstein et al., 2012
CCSM4	H	NCAR, CO, USA	1.1×0.6 (0.3)	1.2×0.9	1/6	Gent et al., 2011
CMCC-CM	I	CMCC, Italia	2.0×1.9 (0.6)	0.7×0.7	1/1	Scoccimarro et al., 2011
CNRM-CM5	J	CNRM-CERFACS, France	1.0×0.8 (0.3)	1.4×1.4	10 /10	Voldoire et al., 2012
CSIRO-Mk3-6-0	K	CSIRO-QCCCE, Australia	1.9×0.9 (0.9)	1.9×1.9	10 /10	Rotstayn et al., 2012 Rotstayn et al., 2010
EC-EARTH	L	EC-EARTH, Europe	1.0×0.8 (0.3)	1.1×1.1	0/2	Hazeleger et al., 2010
FGOALS-g2	M	LASG-CESS, China	1.0×1.0 (0.5)	2.8×2.8	2/3	Yongqiang et al., 2004
FGOALS-s2	N	LASG-IAP, China	1.0×1.0 (0.5)	2.8×1.7	2/3	Yongqiang et al., 2004
FIO-ESM	O	FIO, SOA, China	1.1×0.6 (0.3)	2.8×2.8	1/1	
GFDL-CM3	P	NOAA	1.0×1.0 (0.4)	2.5×2.0	1/5	Donner et al., 2011
GFDL-ESM2G	Q	-GFDL,	1.0×1.0 (0.4)	2.5×2.0	1/3	Donner et al., 2011
GFDL-ESM2M	R	USA	1.0×1.0 (0.4)	2.5×2.0	1/1	Donner et al., 2011
GISS-E2-H	S	NASA/GISS,	2.5×2.0 (2.0)	2.5×2.0	5/5	Schmidt et al., 2006
GISS-E2-R	T	NY, USA	2.5×2.0 (2.0)	2.5×2.0	5/4	Schmidt et al., 2006
HadCM3	U	MOHC, UK	1.2×1.2 (1.2)	3.7×2.5	9/4	Collins et al., 2001
HadGEM2-AO	V	NIMR-KMA,Korea	1.0×1.0 (0.4)	1.9×1.2	1/1	Martin et al., 2011
HadGEM2-CC	W	MOHC, UK	1.0×1.0 (0.4)	1.9×1.2	2/3	Martin et al., 2011
HadGEM2-ES	X	MOHC, UK	1.0×1.0 (0.4)	1.9×1.2	2/3	Collins et al., 2011
INMCM4	Y	INM, Russia	0.8×0.4 (0.4)	2.0×1.5	1/1	Volodin et al., 2010
IPSL-CM5A-LR	Z	IPSL, France	2.0×1.9 (0.6)	3.7×1.9	4/4	Dufresne et al., 2012
IPSL-CM5B-LR	Γ	IPSL, France	2.0×1.9 (0.6)	3.7×1.9	1/1	Dufresne et al., 2012
IPSL-CM5A-MR	Δ	IPSL, France	1.6×1.4 (0.6)	2.5×1.3	1/1	Dufresne et al., 2012
MIROC5	Π	AORI-NIES-	1.6×1.4 (0.6)	1.4×1.4	3/3	Watanabe et al., 2010
MIROC-ESM	Σ	-JAMSTEC, Japan	1.4×0.9 (0.6)	2.8×2.8	3/3	Watanabe et al., 2011
MPI-ESM-LR	Ω	MPI-N, Germany	1.5×1.5 (1.5)	1.9×1.9	3/3	Raddatz et al., 2007
MPI-ESM-MR	@	MPI-N, Germany	0.4×0.4 (0.4)	1.9×1.9	3/3	Raddatz et al., 2007
MRI-CGCM3	#	MRI, Japan	1.0×0.5 (0.5)	1.1×1.1	3/3	Yukimoto et al., 2001
NorESM1-M	$	NCC, Norway	1.1×0.6 (0.3)	2.5×1.9	3/3	
NorESM1-ME	&	NCC, Norway	1.1×0.6 (0.3)	2.5×1.9	1/1	

Table 4: CMIP5 model names; ID for this paper; name of providing institutes; ocean mean zonal resolution (at the equator in °E) × mean 25°N -35°N resolution in latitude (in °), and mean equatorial refinement in brackets (5°S -5°N); atmospheric output resolution (in °E × °N); the number of ensemble members for the Ocean/Atmosphere components is shown in the Ens O/A column.

model name	ID	ensemble members	AMAR -ENSO	LAUS -ENSO	LIND -ENSO
gfdl-cm2-0	g	–	$\surd$	$\surd$	$\surd$
ACCESS-1.0	A	1	$\surd$	$\surd$	$\surd$
CanESM2	D	5	$\surd$	$\surd$	$\surd$
CESM1-CAM5	E	3	$\surd$	$\surd$	$\surd$
CESM1-FASTCHEM	F	0	$\surd$	$\surd$	$\surd$
CCSM4	H	6	$\surd$	$\surd$	$\surd$
CNRM-CM5	J	5	$\surd$	$\surd$	$\surd$
FGOALS-g2	M	–	$\surd$	$\surd$	$\frown$
FGOALS-s2	N	3	$\surd$	$\surd$	$\surd$
FIO-ESM	O	3	$\surd$	$\surd$	$\surd$
GFDL-CM3	P	–	$\frown$	$\frown$	$\surd$
GFDL-ESM2G	Q	–	$\frown$	$\surd$	$\surd$
HadCM3	U	–	$\frown$	$\surd$	$\surd$
HadGEM2-AO	V	1	$\surd$	$\surd$	$\surd$
MIROC5	Π	1	$\surd$	$\surd$	$\surd$
MPI-ESM-LR	Ω	–	$\frown$	$\surd$	$\surd$
MPI-ESM-MR	@	–	$\frown$	$\surd$	$\surd$
NorESM1-M	$	1	$\surd$	$\surd$	$\surd$
NorESM1-ME	&	1	$\surd$	$\surd$	$\surd$

Table 5: List of the CMIP models showing the best skills in term of Indo-Australian monsoon statistical properties. The number of ensemble members used for the assessment of rcp8.5 projections is shown in the third column. The symbol $\surd$ indicates that the specified monsoon-ENSO relationship is well captured, based on criteria described in section 3.2. The symbol $\frown$ indicates a failure in the specified monsoon-ENSO relationship. The models that are removed due to deficiency in the simulated ENSO-monsoon relationship are in italic, the other are in bold.

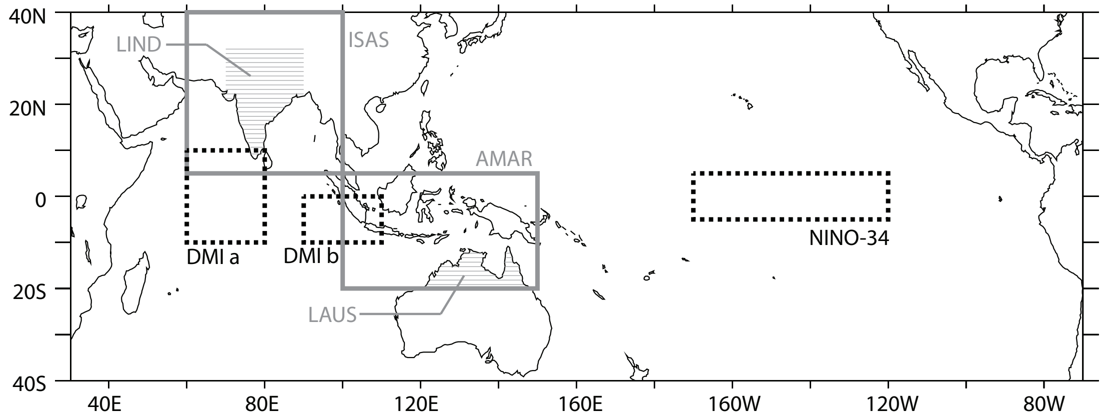

Figure 1: Boxes used to compute indices defined in Tab. 1 (DMI is calculated as DMIa-DMIb), with the shaded areas showing the land-based indices.

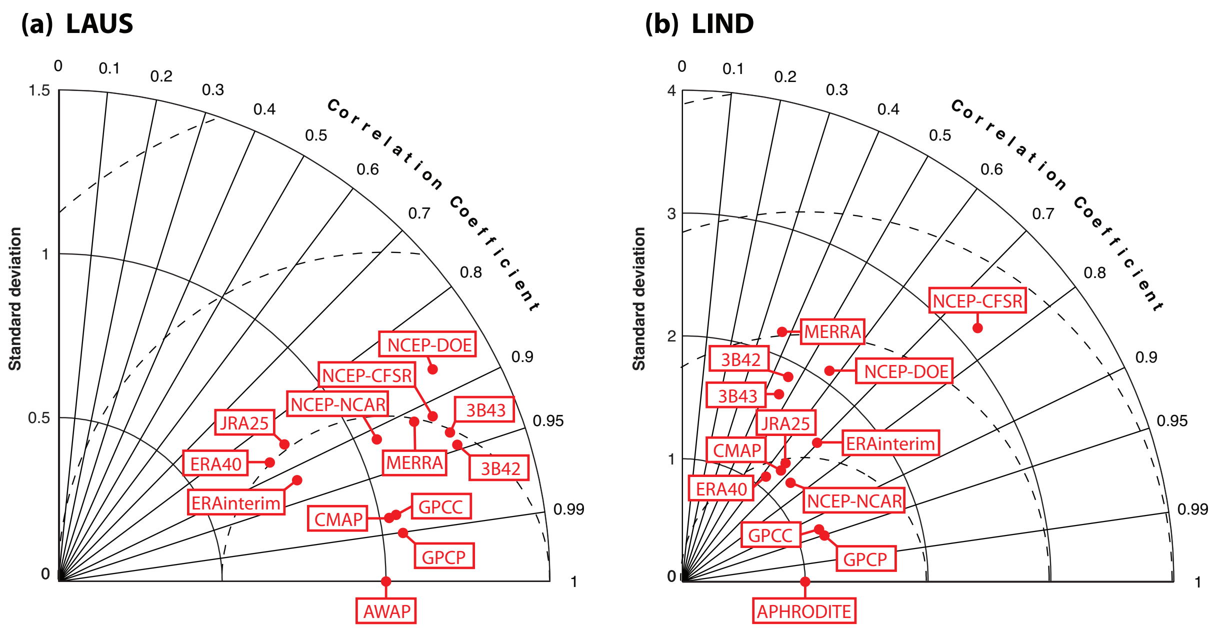

Figure 2: (a) Taylor (2001) diagram for the DJFM Australian monsoon rainfall index (LAUS). (b) same for the JJAS Indian monsoon rainfall index (LIND). One standard deviation unit on the diagram is one standard deviation of AWAP and APHRODITE in Australia and India respectively. Each dataset is compared to AWAP/APHRODITE over the common period (*e.g.* 1948-2009 for NCEP-NCAR but 1998-2009 for TRMM-3B43 in Australia). The distance from AWAP/APHRODITE represents the centered root mean square error as compared to AWAP/APHRODITE (dashed lines, in AWAP/APHRODITE standard deviation units).

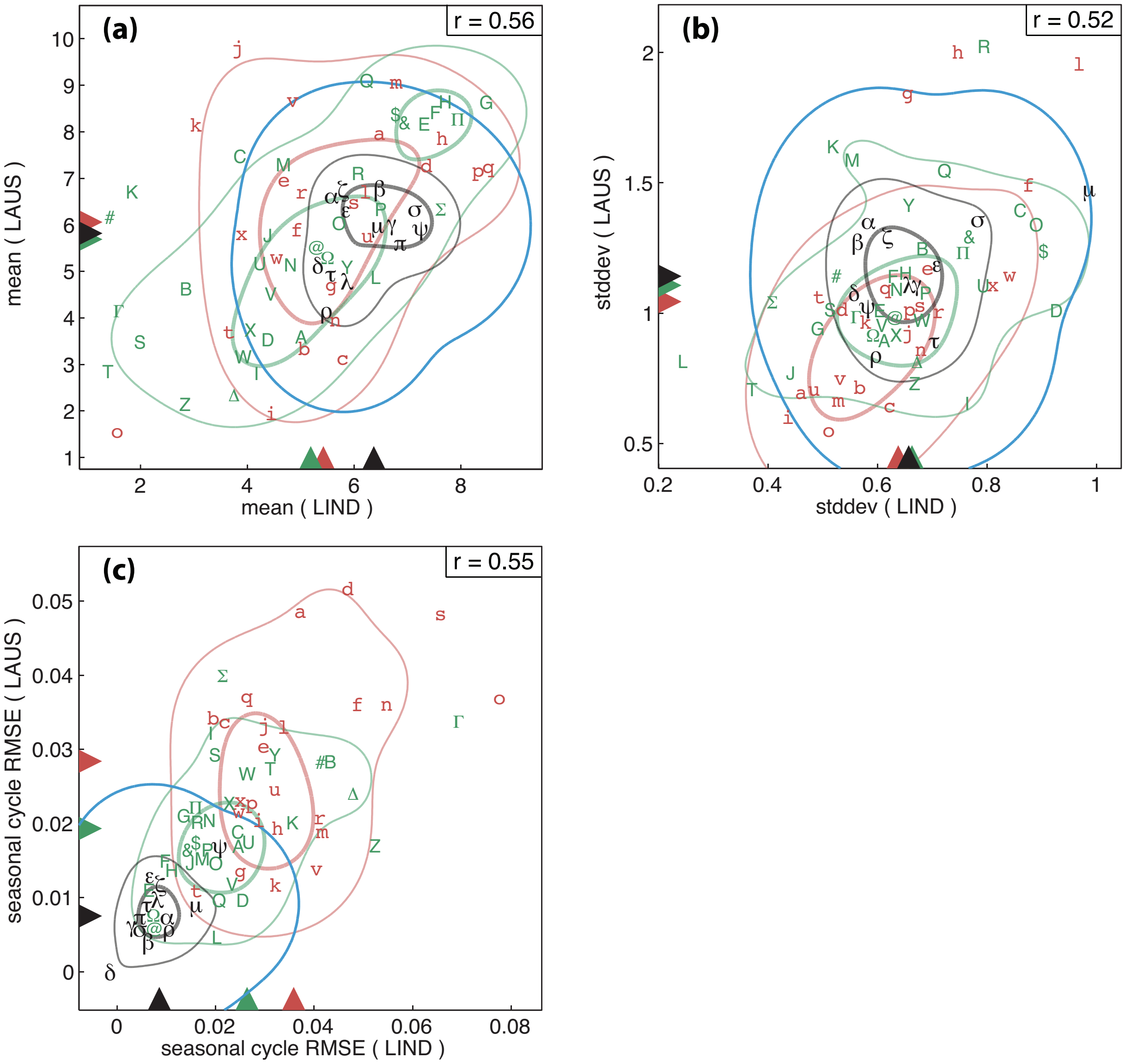

Figure 3: **(a)** mean DJFM Australian monsoon rainfall (LAUS) as a function of mean JJAS Indian monsoon rainfall (LIND). **(b)** Same as (a) but for interannual standard deviations of summer-months-averaged rainfall instead of means. **(c)** RMSE of normalized LAUS seasonal cycles versus RMSE of normalized LIND seasonal cycles, the RMSE being calculated with respect to AWAP in Australia and to APHRODITE in India (see detailed seasonal cycles in Fig. 4). Each letter or symbol refers to a model/dataset from CMIP5 (green, Tab. 4), CMIP3 (red, Tab. 3), or reanalysis/observations (black, Tab. 2). Triangles show the multi-model mean. Units in (a) and (b) are mm/day, while (c) has no units. The number r (upper right of each panel) is the correlation coefficient of the $X - Y$ scatter plot, for CMIP3 and CMIP5 considered together (without observations and reanalysis). The PDF contours are estimated from the sum up of Gaussian functions attributed to each model point. The standard deviation of each individual Gaussian function is chosen as $3s/\sqrt{N}$ in each direction, where s is the standard deviation of one group (CMIP3, CMIP5, or observations/reanalysis), and N the number of elements within the group (such a standard deviation for the Gaussian function enables to fill the average distance between two neighbor points among N points normally distributed). Thick (thin) black, red, and green contours enclose 25% (75%) of PDF integrative. The blue contour encloses 99.9% of the observations/reanalysis PDF integrative in (a) and (b), and 99.999% in (c). In (b), NCEP-DOE-II (represented by μ) and NCEP-CFSR (out of the figure area, standard deviation of 1.5 and 2.0 mm/day for LAUS and LIND respectively) are not considered in the PDF computation. In (c), JRA25 is not considered in the PDF computation.

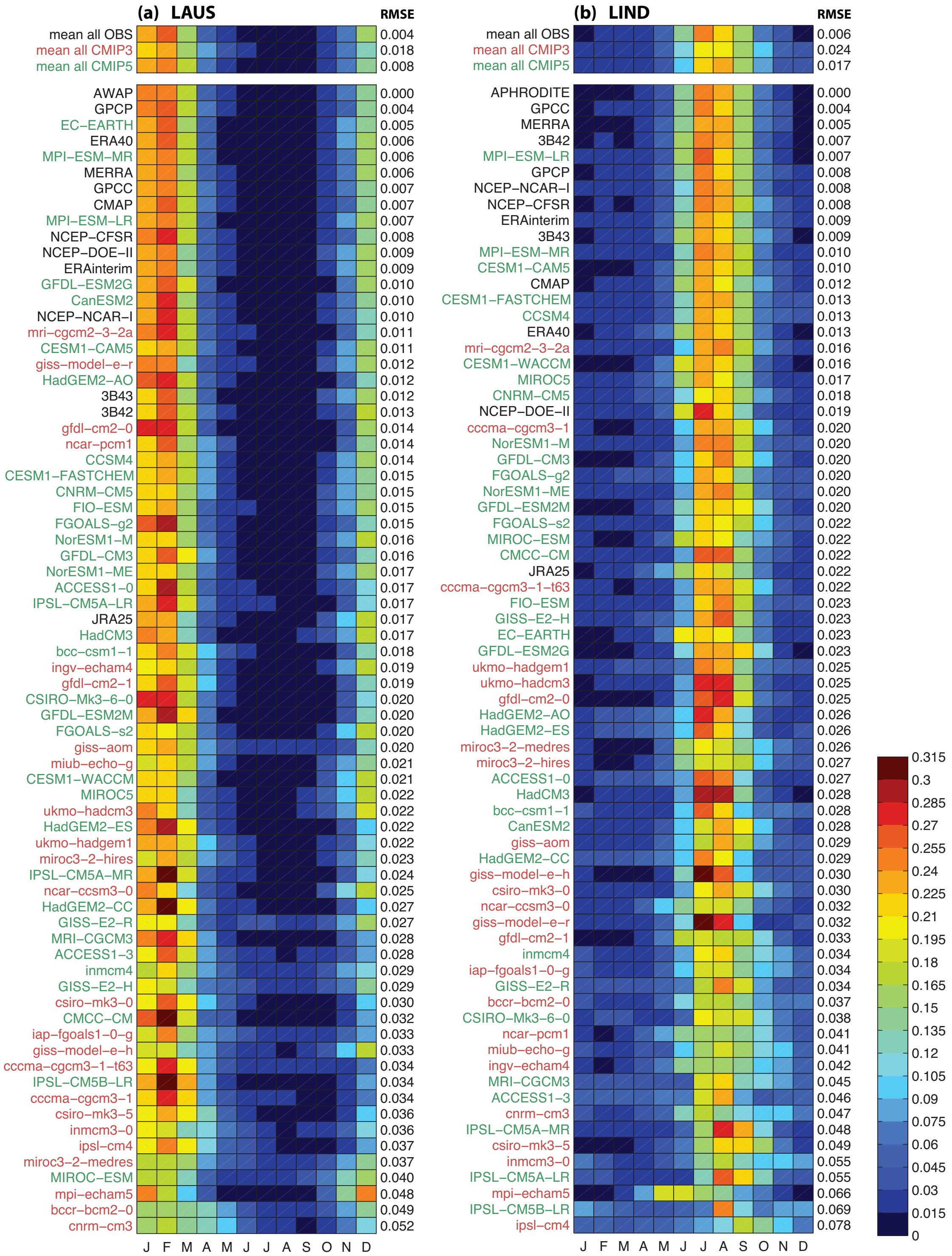

Figure 4: Normalized seasonal cycle of LAUS **(a)** and LIND **(b)**, for observations/reanalysis (black), CMIP3 (red) and CMIP5 (green), and sorted by increasing RMSEs (shown on the right of each panel, and computed with regards to AWAP in Australia and to APHRODITE in India).

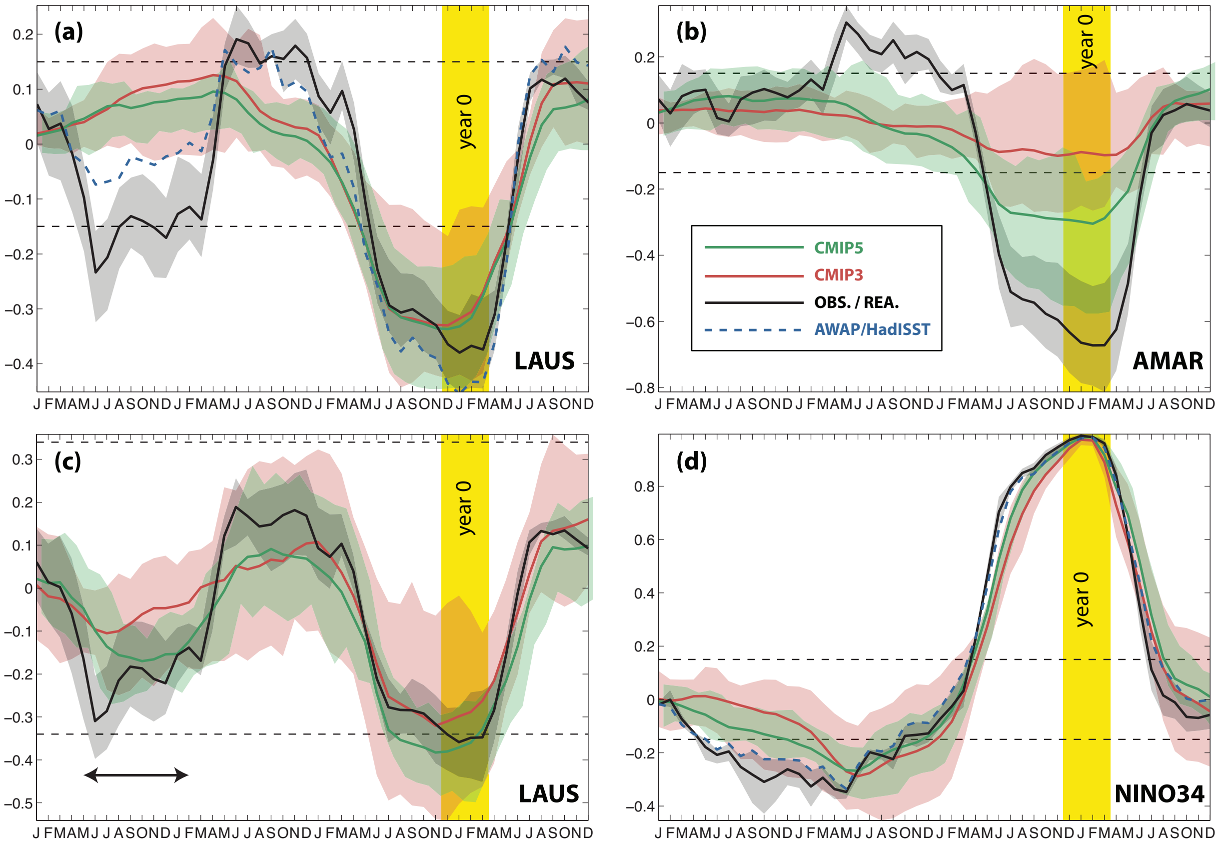

Figure 5: **(a)** Lag correlation between LAUS averaged in DJFM of year 0 and monthly NINO34 values (months on the X-axis). Thick lines are the means over the observations/reanalysis (black), CMIP3 (red), and CMIP5 (green). Semi-transparent areas show the upper and lower quartiles. The dashed blue thick line in (a) and (d) represents AWAP-HadISST. The yellow area indicates the reference time (t=0), and its width shows the DJFM months over which each index is averaged. **(b)** Same as (a) but for AMAR instead of LAUS. **(c)** Same as (a), but selecting the 30 year period of each model (over the 150 years of each member and among the ensemble members) that gives the strongest anti-correlation over the period shown by the black double arrow. **(d)** Same as (a) but for NINO34 instead of LAUS.

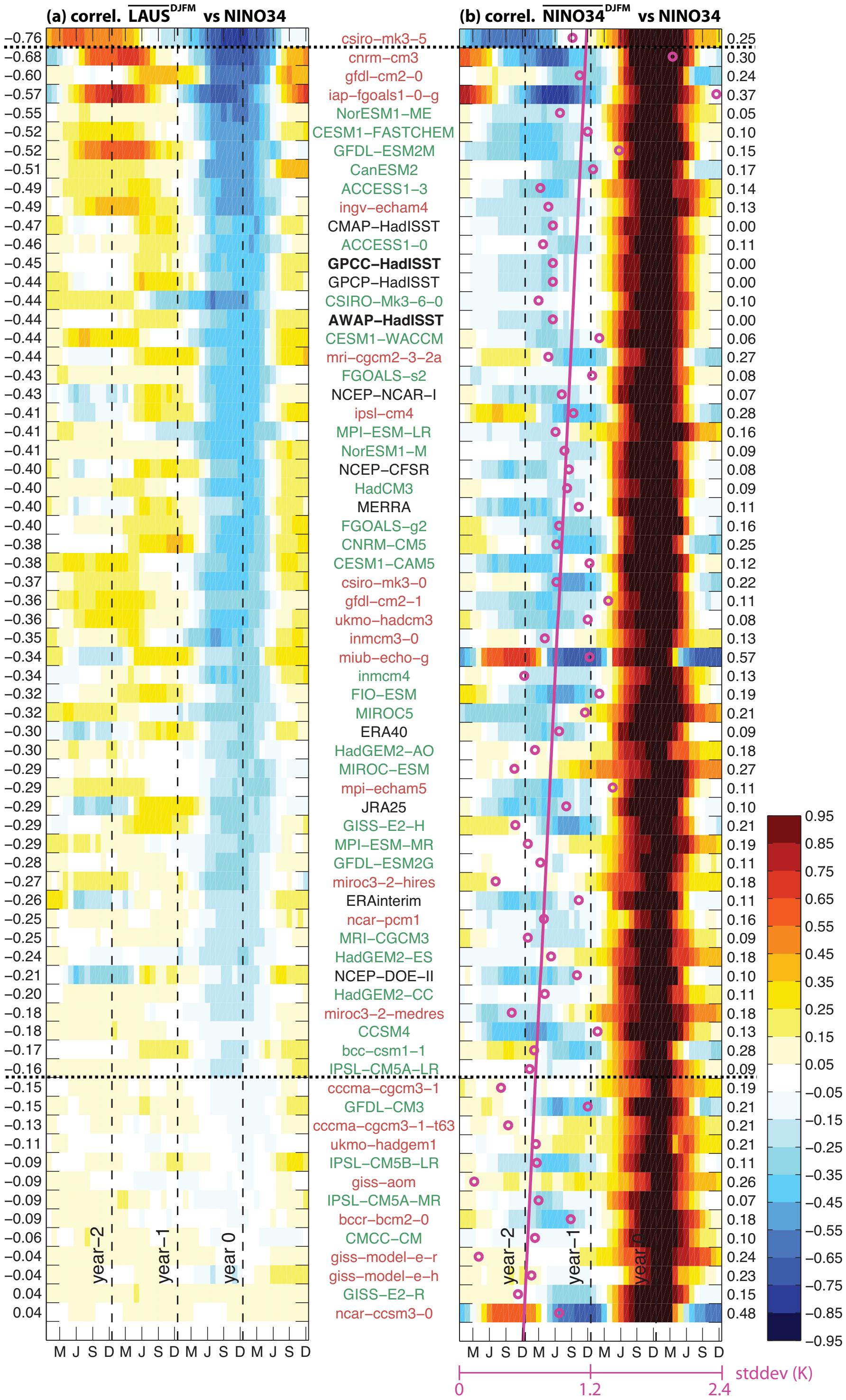

Figure 6: **(a)** Lag correlation between LAUS averaged in DJFM of year 0 and monthly NINO34 values (months on the X-axis, M for March and J for June) for observations/reanalysis (black names), CMIP3 (red), and CMIP5 (green) ranked by increasing correlation in year0 DJFM. **(b)** Same as (a) but for correlation between NINO34 averaged in DJFM and lagged monthly NINO34 values. Pink circles indicate the standard deviation of NINO34 produced by each model. The pink line is the least mean square linear fit of these circles (correlation=0.45).

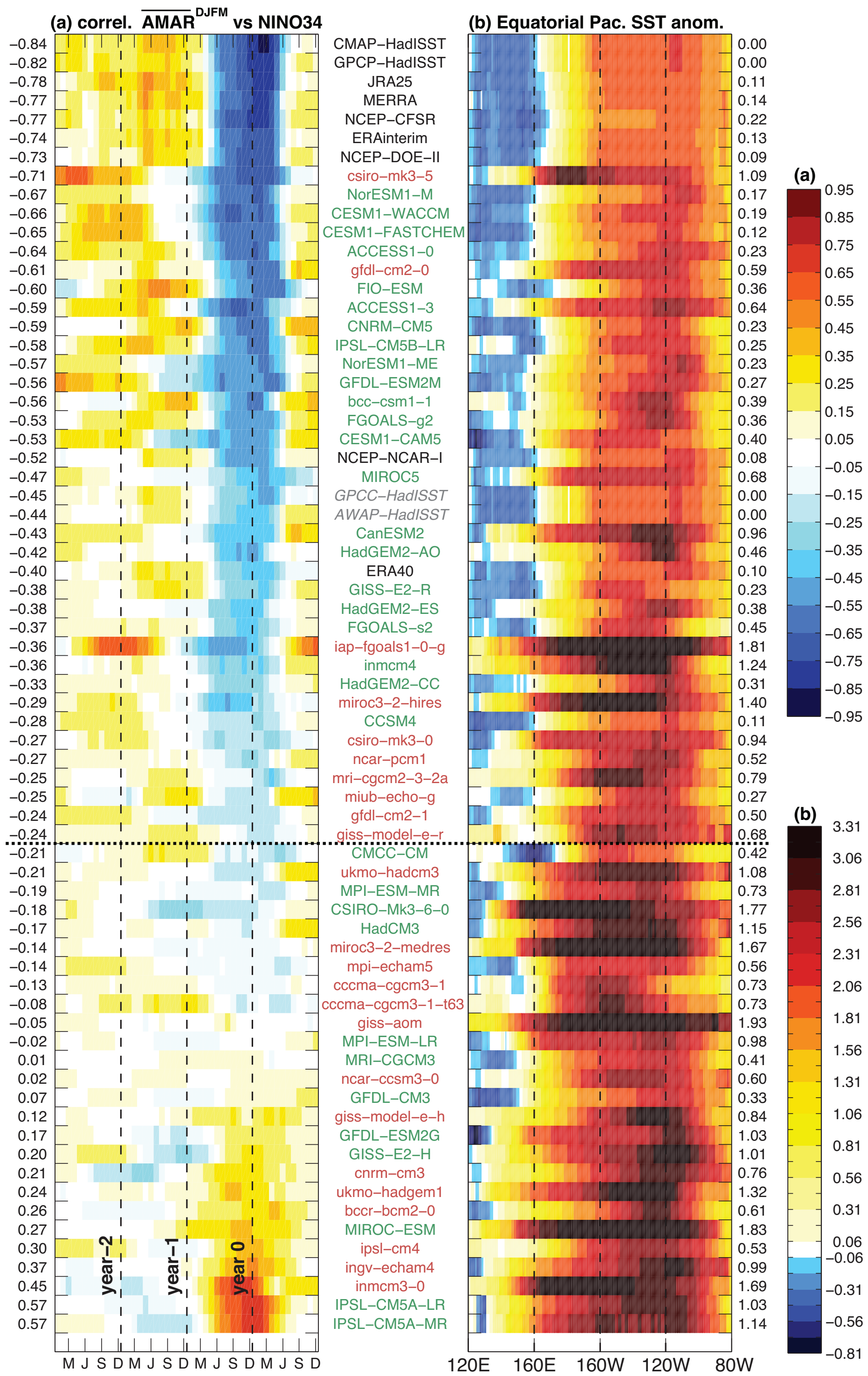

Figure 7: **(a)** Lag correlation between AMAR averaged in DJFM of year 0 and monthly NINO34 values (months on the X-axis, M for March and J for June) for observations/reanalysis (black names), CMIP3 (red), and CMIP5 (green) ranked by increasing correlation in year0 DJFM (indicated on the left hand side). Names of land-only data are in gray. **(b)** Composite of equatorial Pacific SST anomalies (5°N -5°S average, in K) for NINO34 greater than 1 standard deviation. The RMSE with regards to HadISST is indicated on the right hand side.

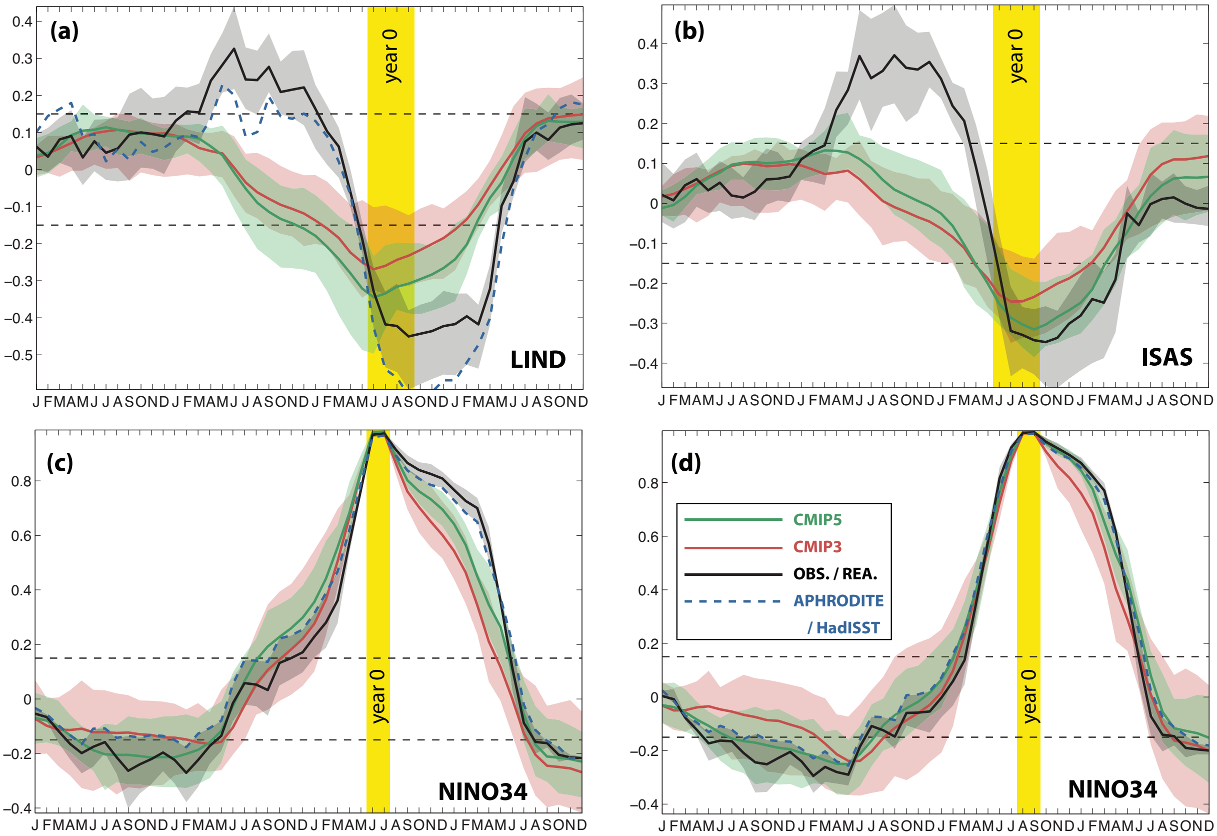

Figure 8: **(a)** Lag correlation between LIND averaged in JJAS of year 0 and monthly NINO34 values (months on the X-axis). Thick lines are the means over the observations/reanalysis (black), CMIP3 (red), and CMIP5 (green). Semi-transparent areas show the upper and lower quartiles. The dashed blue thick line represents APHRODITE-HadISST. The yellow area indicates the reference time (t=0), and its width shows the JJAS months over which each index is averaged. The black dashed lines represent the 90% significance of correlation coefficients for a single time-series of 150 years (see caption of Fig. 5). **(b)** Same as (a) but for ISAS instead of LIND. **(c)** Same as (a) but for June-July NINO34 instead of JJAS LIND. **(d)** Same as (c) but for August-September NINO34.

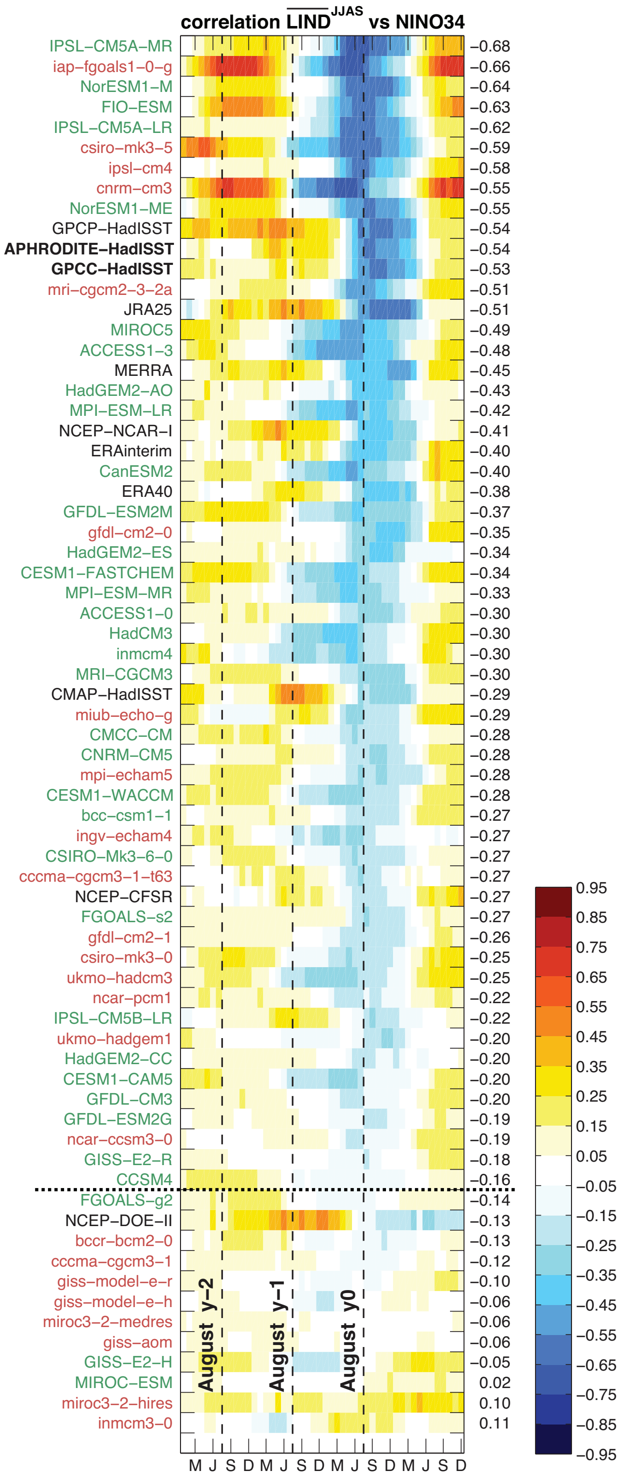

Figure 9: Lag correlation between LIND averaged in JJAS of year 0 and monthly NINO34 values (months on the X-axis, M for March and J for June) for observations/reanalysis (black names), CMIP3 (red), and CMIP5 (green) ranked by increasing correlation in year0 JJAS.

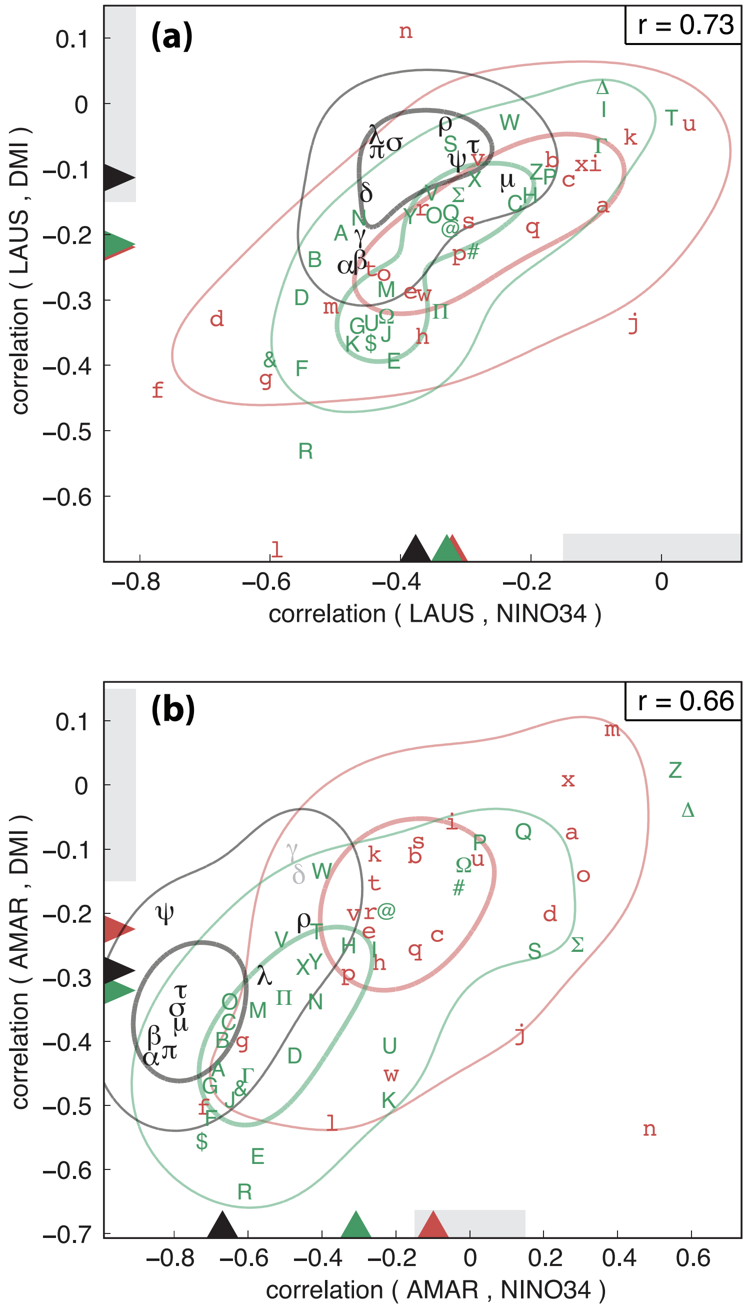

Figure 10: **(a)** Scatter plot of the correlation between SON DMI and DJFM LAUS (Y-axis) as a function of the correlation between DJFM NINO34 and DJFM LAUS (X-axis). Envelopes are PDF contours (see Fig. 3). Multi-model means are shown by triangles. Gray bars along the axis show correlation values that are below the 90% significance level for a 150-year time series. **(b)** Same but with AMAR instead of LAUS, with land-based observations represented by gray letters.

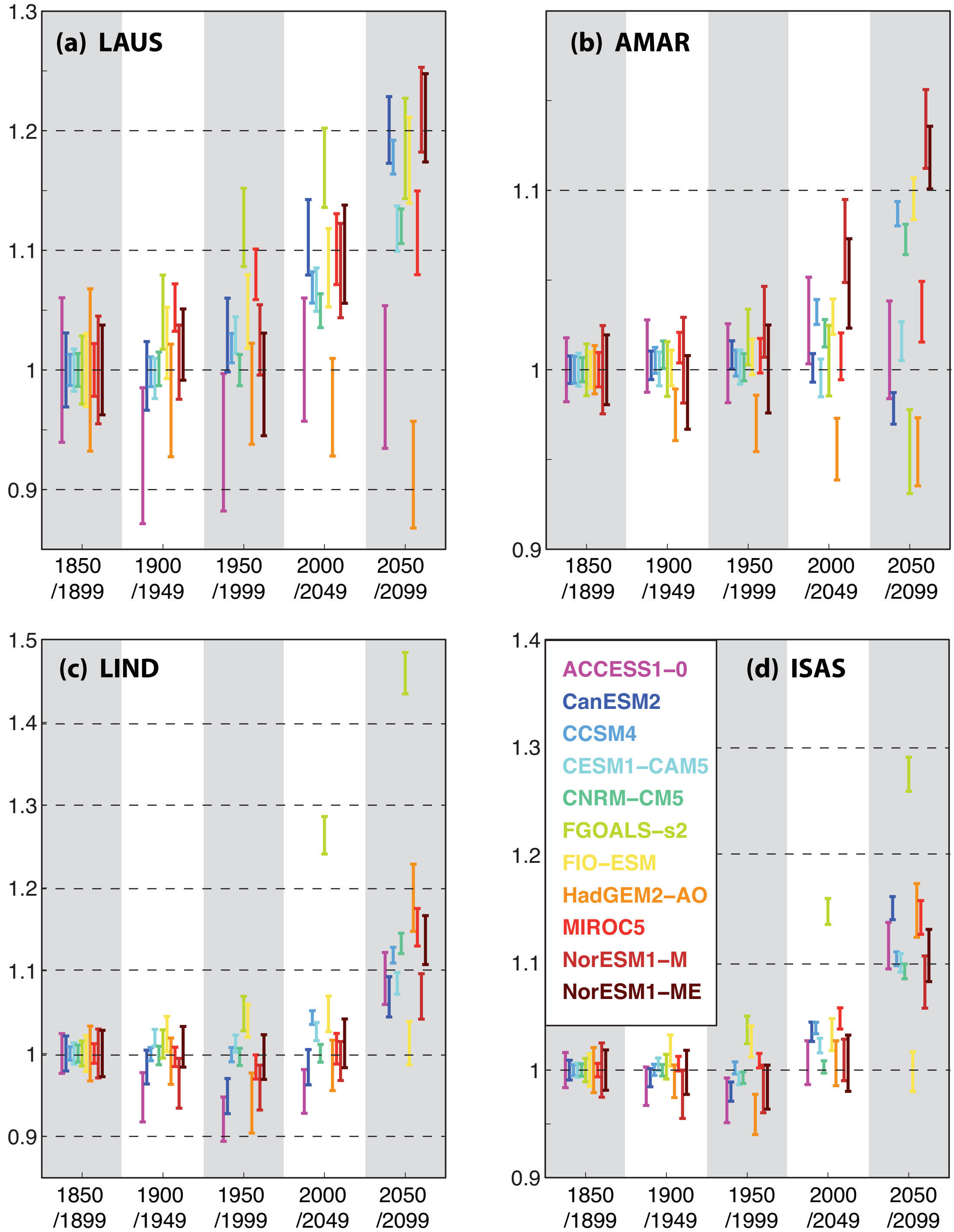

Figure 11: Summer monsoon rainfall averaged over 50-year periods and divided by the 1850-1899 mean for LAUS (a), AMAR (b), LIND (c), and ISAS (d). Error bars show the confidence interval at the 90% level (the uncertainty of the denominator not taken into account, so that bars have to be compared to each others rather than to unity).

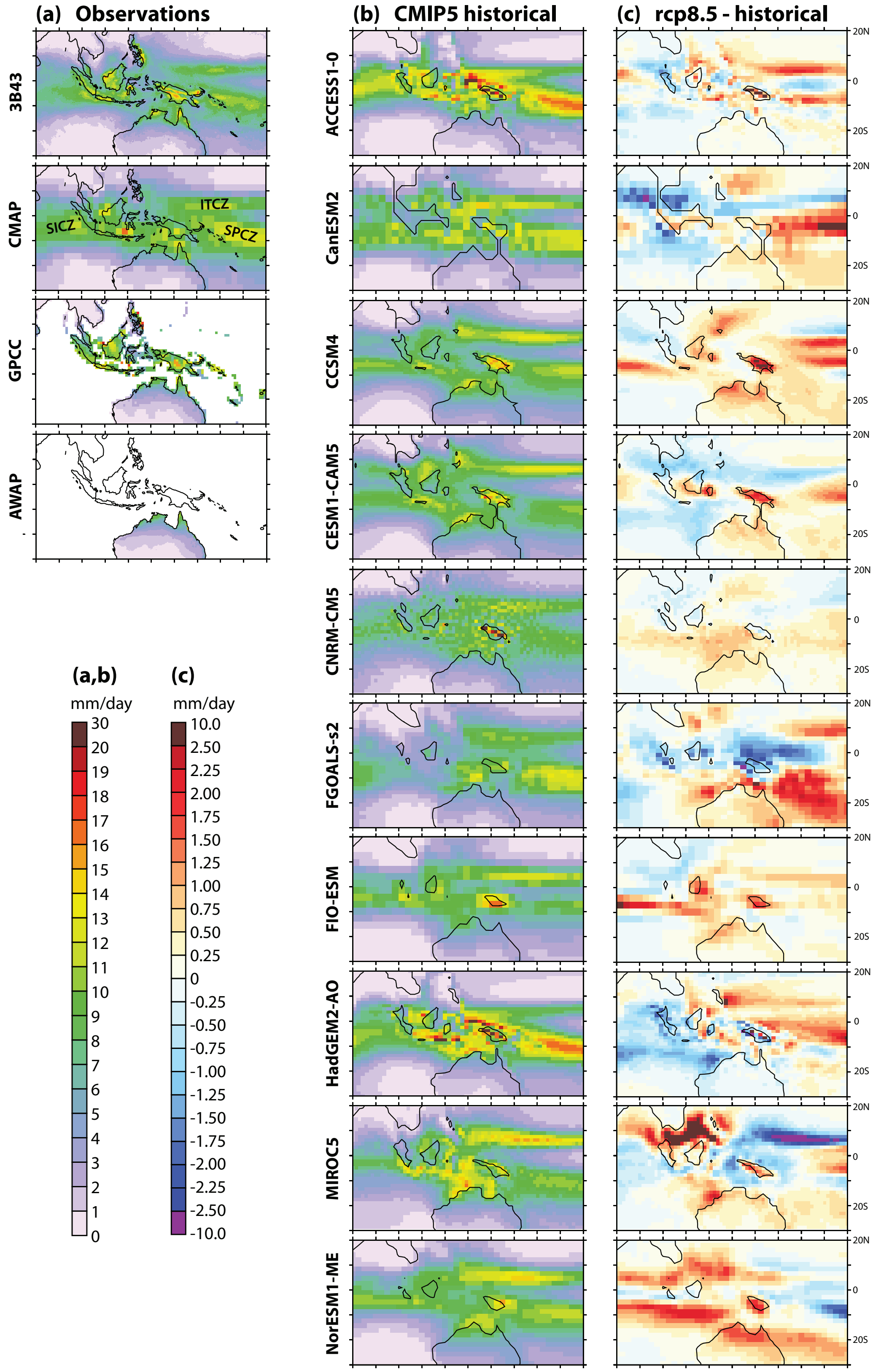

Figure 12: DJFM rainfall in the observations (a) and in the historical CMIP5 simulations (b), and difference between the 2006-2100 mean rainfall from rcp8.5 experiments and the 1850-2005 mean rainfall (c). Maps from NorESM1-M are not shown since they are quite similar to the map from NorESM1-ME.

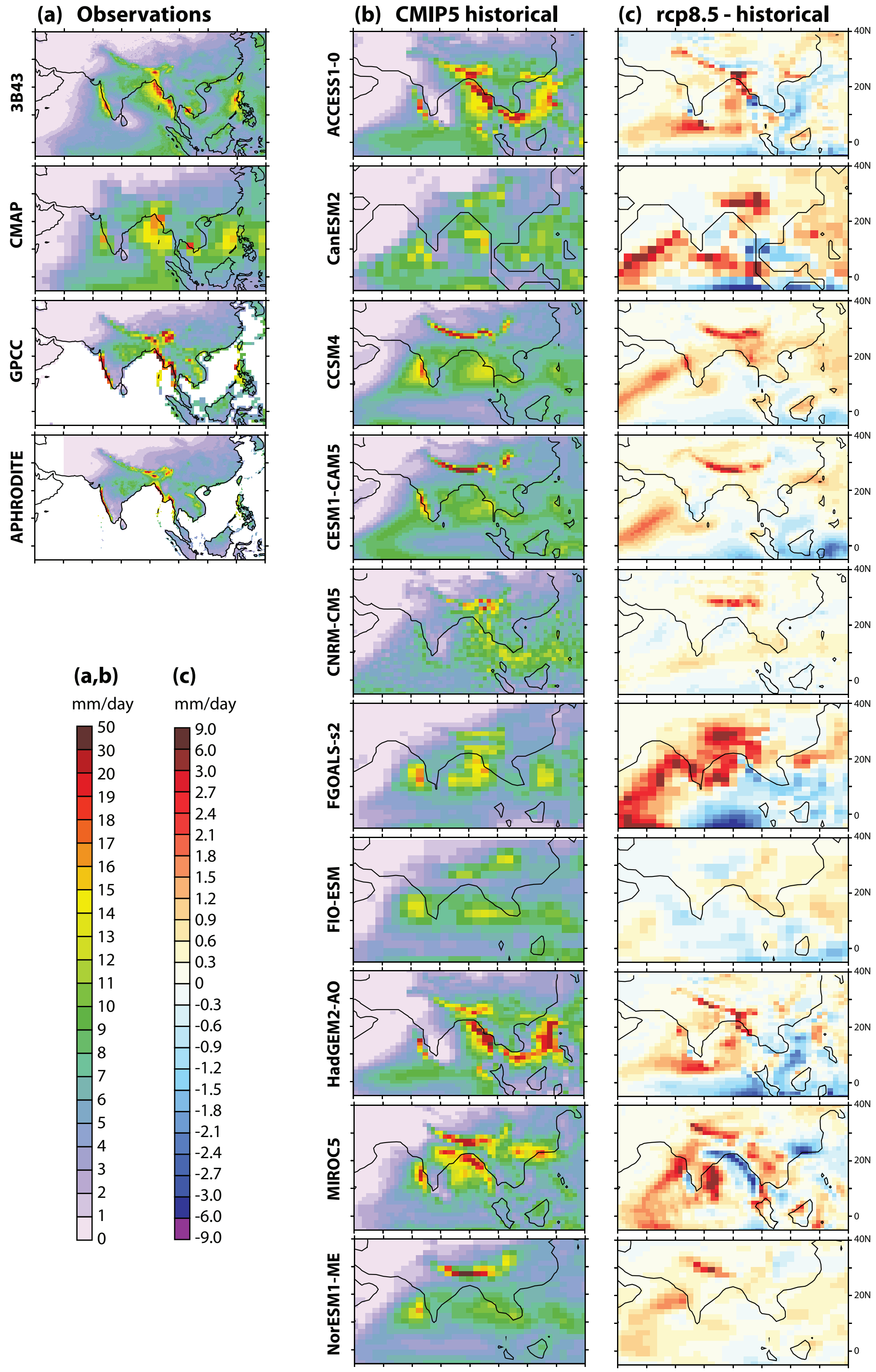

Figure 13: JJAS rainfall in the observations (a) and in the historical CMIP5 simulations (b), and difference between the 2006-2100 mean rainfall from rcp8.5 experiments and the 1850-2005 mean rainfall (c). Maps from NorESM1-M are not shown since they are quite similar to the map from NorESM1-ME.